Mathematical Biosciences and Engineering

https://www.aimspress.com/journal/mbe

MBE, 23(6): 1799–1843.
DOI: 10.3934/mbe.2026066
Received: 13 April 2026
Revised: 02 May 2026
Accepted: 12 May 2026
Published: 22 May 2026

Research article

Delayed immune responses and heterogeneous exposure shape within-host viral dynamics

Abdelkarim Lamghari[1,*] **and Aissam Jebrane**[2]

[1] LAMAI, Faculty of Sciences and Technics, Department of Mathematics, Cadi Ayyad University, Marrakesh 40140, Morocco

[2] École Centrale Casablanca, Complex Systems and Interactions Research Center (CSIRC), Ville Verte, Bouskoura 27182, Morocco

* **Correspondence:** Email: abdelkarimsm@gmail.com.

Abstract: In this paper, we present a delayed within-host viral dynamics model that integrates nonlinear immune responses and heterogeneous exposure. The model combines logistic viral replication, delayed immune-mediated clearance, and time-dependent external forcing. We introduce a 4×4 factorial framework that systematically couples four canonical immune response architectures (linear, Michaelis–Menten, Hill-type, and switch-like) with four representative exposure profiles (constant, periodic, event-driven, and adaptive), yielding sixteen distinct dynamical scenarios. A rigorous theoretical analysis established positivity, boundedness, equilibrium structure, and delay-induced Hopf bifurcations. Extensive numerical simulations quantified transient amplification, timing, clearance efficiency, oscillatory behavior, and long-term persistence using a comprehensive set of nine quantitative metrics. The results reveal robust dynamical hierarchies governed by immune sensitivity and exposure intermittence rather than maximal clearance capacity. In particular, ultrasensitive immune responses amplified early overshoots and cumulative burden, whereas impulsive or adaptive exposure substantially reduced persistence and accelerated post-peak decay. These findings revealed fundamental trade-offs between early transient control and long-term viral persistence in delayed immune feedback systems.

Keywords: within-host viral dynamics; immune delay; nonlinear immune response; external forcing; delay differential equations; Hopf bifurcation

1. Introduction

Within-host viral dynamics arise from the interplay between viral replication, immune-mediated clearance, and external exposure [1,2]. Immune responses are characterized not only by their functional

architecture but also by activation delays reflecting recognition, signaling, and effector deployment. These delays can substantially alter infection dynamics, leading to transient overshoots, oscillations, or sustained viral persistence.

Such dynamics have been extensively studied in the context chronic and acute infections, including HIV and COVID-19 [1–3]. The classical target-cell limited framework, introduced by Nowak and May and supported by Perelson and collaborators, provides a quantitative basis for describing viral replication, infected cell lifespan, and clearance kinetics [1, 2]. It has been shown that viral populations exhibit rapid turnover, indicating the central role of immune-mediated mechanisms in infection control [3].

Further studies have incorporated immune responses more explicitly. In particular, nonlinear mechanisms such as saturation and density-dependent killing have been shown to be necessary to reproduce observed infection dynamics [4, 5]. In addition, biological delays arising from intracellular viral production and immune activation processes have been modeled using delay differential equations [2]. These studies suggest that delays can generate oscillations and modify equilibrium stability, leading to qualitatively different infection dynamics [6, 7].

Moreover, within-host viral dynamics have been revisited from a rigorous mathematical perspective, with particular emphasis on structural properties such as positivity, boundedness, and global stability of equilibria [8].

In parallel, researchers have explored more biologically detailed formulations incorporating heterogeneous transmission and immune response variability [9–11]. Delay differential equation frameworks have been widely employed to capture immune activation lags and their dynamical consequences, including oscillatory behavior and stability shifts [12–15]. Empirical and epidemiological studies further highlight the importance of viral load kinetics and transmission heterogeneity in shaping infection outcomes [16–18]. However, most approaches treat delayed immune responses and time-dependent exposure separately, leaving their combined impact insufficiently understood.

From a modeling perspective, exposure is inherently time-dependent. Contact patterns, social behavior, and environmental conditions generate repeated, periodic, or sporadic viral intake, especially for respiratory infections. Moreover, multiscale studies highlight the importance of time-varying exposure for infection kinetics [19–21]. Specifically, choosing the appropriate mathematical framework to capture these dynamics is essential for accurate predictions [22], and understanding immune dysregulation remains a cornerstone of modern within-host modeling [23]. However, most within-host models either neglect such forcing or examine it independently of immune nonlinearity.

Experimental evidence further indicates that the timing of immune activation is a key determinant of infection outcomes. In infections, such as influenza and COVID-19, early immune activation is associated with faster viral clearance, whereas delayed responses are linked to higher viral loads and prolonged infection [24–26].

In this work, we aim to develop a unified framework that jointly accounts for delayed immune responses and heterogeneous exposure. We compare four canonical immune response architectures with four representative exposure profiles, leading to sixteen distinct scenarios. Using analytical tools for delay differential equations and a comprehensive numerical study, we characterize how immune architecture and exposure structure jointly determine infection severity, timing, clearance efficiency,

and oscillatory behavior.

While delay-induced oscillations and Hopf bifurcations are well-characterized in within-host modeling, their interaction with heterogeneous exposure remains less explored.

We extend classical stability analysis by systematically coupling delayed immune feedback with time-dependent exposure. We introduce a 4×4 factorial framework comprising sixteen dynamical scenarios to investigate how nonlinearity and exposure structure co-determine transient amplification, oscillatory regimes, and viral persistence.

These four immune response functions are selected as canonical representations spanning linear, saturating, cooperative, and threshold-driven activation mechanisms widely reported in immunological modeling. Similarly, the chosen exposure profiles capture persistent, periodic, impulsive, and feedback-regulated contact patterns, thereby providing a minimal yet comprehensive basis for systematically exploring the interaction between immune dynamics and heterogeneous exposure.

The remainder of this paper is organized as follows. In Section 2, we introduce the mathematical model, detailing the four immune response functions and the four exposure profiles. In Section 3, we provide a rigorous theoretical analysis, including proofs for existence, uniqueness, and stability under different exposure regimes. In Section 4, we describe the numerical methodology and the quantitative metrics used for comparison. Results and discussion are presented in Sections 5 and 6, while in Section 7, we conclude the paper with biological implications and future directions.

2. Mathematical model

The within-host viral dynamics are described by the following delay differential equation:

$$\frac{dC(t)}{dt} = r\,C(t)(1 - C(t)) + \rho\,C_a(t) - \gamma\,C(t)\,f(C(t-\tau))\,, \tag{2.1}$$

where $C(t)$ denotes the viral load at time t. The model accounts for intrinsic viral replication, external exposure, and immune-mediated clearance. Viral replication is subject to saturation effects reflecting finite within-host resources. External exposure is represented by the time-dependent forcing term $C_a(t)$, which reflects social interactions, contact frequency, and the nature of contacts, thereby capturing repeated or sustained exposure to infectious sources. Immune clearance depends on past viral load levels, incorporating the delayed activation of the immune response.

Parameter r denotes the intrinsic replication rate, ρ scales the contribution of external exposure, and γ quantifies immune efficiency. The delay τ represents the time required for immune activation, while function $f(\cdot)$ specifies the dependence of immune response on previous viral load.

Assumption 1 (Parameter admissibility)**.** All model parameters are assumed to be non-negative and biologically meaningful. In particular,

$$r > 0, \quad \gamma > 0, \quad \rho \geq 0, \quad \tau \geq 0,$$

and all parameters appearing in the immune response functions (e.g., K, n, κ, C^*) are strictly positive.

These assumptions are used throughout the analysis to ensure positivity, boundedness, and well-posedness of the system. The parameters introduced in Eq (2.1) are selected to be biologically plausible and consistent with reported ranges in within-host viral dynamics studies.

2.1. Immune response functions

To investigate how immune activation mechanisms shape within-host viral dynamics, we consider four canonical immune response functions commonly employed in the literature [1, 2]. These functions capture different levels of biological complexity, ranging from proportional clearance to saturating, cooperative, and threshold-driven immune responses. All functions $f(C)$ are assumed to be monotonically non-decreasing and bounded, ensuring biologically plausible immune-mediated clearance rates [**?**].

Table 1. Immune response functions considered in the model and their biological interpretation.

Response type	Functional form $f(C)$	Biological interpretation
Linear	C	Proportional immune clearance; baseline reference
Michaelis–Menten	$\dfrac{C}{K+C}$	Saturating response due to limited effector capacity
Sigmoidal (Hill)	$\dfrac{C^n}{K^n+C^n}$	Cooperative activation and ultrasensitivity
Switch-like	$\dfrac{1}{1+\exp[-\kappa(C-C^*)]}$	Threshold-dependent, all-or-none immune activation

A graphical illustration of the immune response functions is provided in Figure 1(A).

The linear response represents the simplest formulation of immune-mediated clearance, in which immune activity increases proportionally with viral load. Owing to its analytical tractability, this form is frequently adopted as a baseline in within-host viral models and serves as a reference for stability and persistence analyses [1, 2].

The Michaelis–Menten formulation introduces saturation effects, reflecting biological constraints such as finite numbers of cytotoxic lymphocytes or limited killing capacity. This functional form has been widely used to model viral–immune interactions and captures the empirically observed decrease in marginal immune efficiency at high viral loads [**?**, 28].

The Hill-type sigmoidal response generalizes the Michaelis–Menten formulation by incorporating cooperative effects. For Hill coefficients $n > 1$, immune activation becomes ultrasensitive, enabling the model to reproduce sharp transitions between weak and strong immune clearance. Such behavior is consistent with cooperative molecular binding and signaling cascades involved in immune activation [29].

Finally, the switch-like response explicitly models threshold-dependent immune activation. Parameter C^* represents the viral load required to trigger a substantial immune response, while κ controls the steepness of this transition. This formulation is particularly suitable for immune processes exhibiting abrupt activation, such as T-cell responses and regulatory feedback mechanisms, and enables the study of bistability and sudden immune onset in within-host dynamics [30].

Each immune response function listed in Table 1 can be substituted into Eq (2.1), yielding distinct immune-mediated clearance dynamics. This comparative framework enables us to assess how the functional architecture of immune activation influences viral persistence, clearance, and transient behavior. The explicit analytical forms and parameter values used for all immune response functions are summarized in Appendix (Table A2).

2.2. *Exposure functions*

To represent heterogeneous interactions between the host and the viral environment, we introduce a set of time-dependent exposure functions $C_a(t)$ acting as external forcing terms in Eq (2.1). These functions encode the temporal structure of environmental exposure resulting from social interactions, contact frequency, and the nature of contacts. Similar forcing approaches have been widely used in within-host and multiscale models to couple individual-level viral dynamics with population-level or behavioral processes [2, 19, 20].

We consider four representative exposure formulations, constant, periodic, event-driven, and adaptive, which capture a broad spectrum of realistic contact patterns. These formulations are summarized in Table 2.

The corresponding exposure profiles are illustrated in Figure 1(B), highlighting differences in persistence, periodicity, and impulsive forcing.

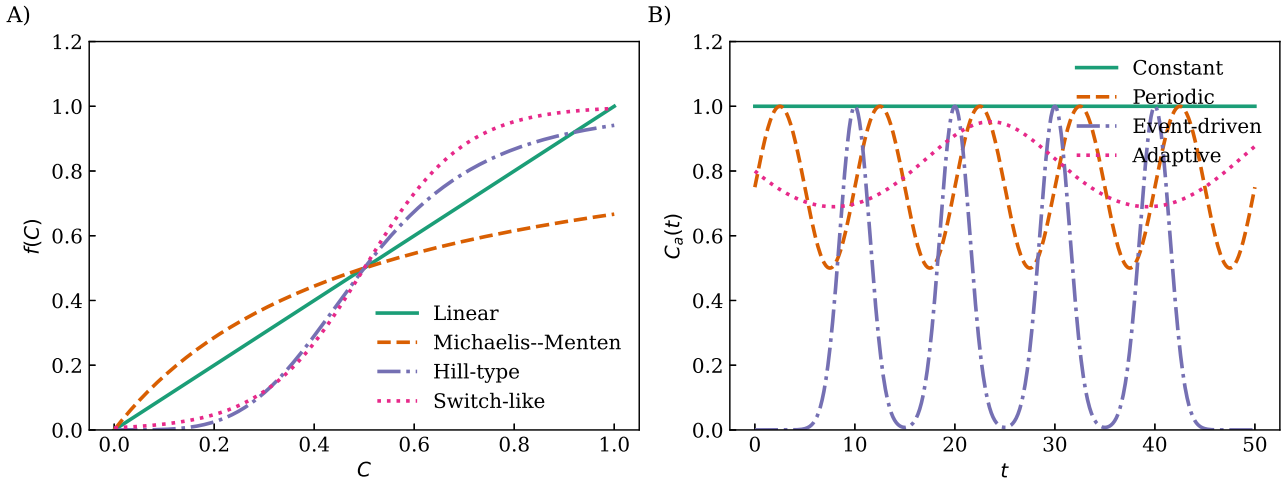

Figure 1. (A) Immune response functions $f(C)$: Linear, Michaelis–Menten, Hill-type, and switch-like, with distinct levels of saturation, cooperativity, and threshold effects. (B) Exposure profiles $C_a(t)$: Constant, periodic, event-driven, and adaptive, with different temporal patterns of environmental viral input. These functions and profiles define the dynamical configurations of the model (Eq (2.1)). Unless otherwise specified, parameters are set to the baseline values in Table 3.

Table 2. Exposure functions considered in the model and their interpretation.

Exposure type	Mathematical form $C_a(t)$	Interpretation
Constant	$C_a = C_0$	Persistent background exposure
Periodic	$C_0\left(1 + \frac{1}{2}\sin(\omega t)\right)$	Regular or seasonal contact patterns
Event-driven	$\sum_{t_e \in \mathcal{T}} A \exp\left(-\frac{(t-t_e)^2}{2\sigma^2}\right)$	Discrete exposure events or gatherings
Adaptive	$\frac{C_0}{1 + \alpha\, C(t)}$	Behavioral response to infection level

The constant exposure function represents sustained background contact with the viral environment, corresponding to continuous low-level exposure through routine social interactions. This formulation is commonly adopted as a baseline forcing term in within-host and hybrid models [1, 2].

The periodic exposure function captures regular fluctuations in contact intensity, such as daily, weekly, or seasonal variations in social behavior. Periodic forcing has been extensively used in epidemiological and multiscale models to represent structured contact patterns and has been shown to generate nontrivial dynamical behaviors, including resonance and oscillations [31, 32].

The event-driven formulation models discrete exposure episodes, such as mass gatherings, high-risk encounters, or sporadic environmental contamination. Gaussian pulses provide a smooth representation of temporally localized exposure events and have been employed in within-host and population-level models to represent impulsive or clustered transmission events [21, 33].

Finally, the adaptive exposure function introduces feedback between the viral load and contact behavior. Parameter α quantifies the strength of behavioral adaptation, such as self-isolation or reduced social activity in response to increasing infection burden. Similar adaptive formulations have been proposed in behavioral epidemiology and multiscale frameworks to account for risk-aware contact modulation and feedback-driven dynamics [19, 34]. The normalized mathematical expressions of all exposure profiles used in numerical simulations are provided in Appendix (Table A1).

3. Theoretical analysis and analytical foundations

3.1. Mathematical preliminaries

In this section, we introduce the functional framework and analytical tools used throughout the paper. Only results that are directly applied in the subsequent analysis are presented.

3.1.1. Phase space and well-posedness

Let $\tau > 0$ and define the phase space

$$\mathcal{X} := C([-\tau, 0], \mathbb{R}), \qquad \|\phi\|_\infty := \sup_{\theta \in [-\tau, 0]} |\phi(\theta)|.$$

Here, $\mathcal{X} = C([-\tau, 0], \mathbb{R})$ denotes the Banach space of continuous functions defined on $[-\tau, 0]$, equipped with the supremum norm.

For a solution $C(t)$, the associated history segment is defined by

$$C_t(\theta) := C(t+\theta), \qquad \theta \in [-\tau, 0].$$

Theorem 3.1 (Existence and uniqueness)**.** See [35, Chapter 2, Section 2.2] and [36, Chapter 2, Section 2.2]. *Consider*

$$\frac{dC(t)}{dt} = r\,C(t)(1 - C(t)) - \gamma\,C(t)\,f(C(t-\tau)) + \rho\,C_a(t).$$

If f is locally Lipschitz and $C_a(t)$ is continuous, then for any initial function $\phi \in \mathcal{X}$, there exists a unique classical solution $C(t)$ defined on a maximal interval $[0, T_{\max})$.

Proposition 3.2 (Semiflow well-definedness [36, Chapter 3, Sections 3.1–3.2])**.** *Under the assumptions of Theorem 3.1, the solution map*

$$T(t)\phi := C_t(\cdot), \qquad t \geq 0,$$

defines a continuous semiflow on $\mathcal{X}$:

$$T(0) = I, \qquad T(t+s) = T(t) \circ T(s), \qquad T(t)\phi \text{ depends continuously on } (\phi, t).$$

Lemma 3.3 (Forward invariance [35, Chapter 2, Section 2.3]; [36, Chapter 4, Section 4.2])**.** *For any initial history function $\phi \in C([-\tau, 0], [0, 1])$, the corresponding solution $C(t)$ of the system remains in $[0, 1]$ for all $t \geq 0$.*

Proof. The result follows from standard comparison arguments and the positive invariance of $[0, 1]$, since the vector field points inward at the boundaries $C = 0$ and $C = 1$.

Theorem 3.4 (Razumikhin stability theorem [36, Chapter 5, Section 5.4]; [35, Chapter 2, Section 2.6])**.** *Let $V : \mathbb{R} \to \mathbb{R}_+$ be a continuously differentiable function. Assume that there exist constants $c_1, c_2, c_3 > 0$ and $q > 1$ such that*

$$c_1|x|^2 \leq V(x) \leq c_2|x|^2,$$

and whenever the condition

$$V(x(t+\theta)) \leq qV(x(t)), \quad \forall \theta \in [-\tau, 0]$$

is satisfied, we have

$$\dot{V}(x(t)) \leq -c_3|x(t)|^2.$$

Then the equilibrium $x = 0$ is globally asymptotically stable.

3.1.2. Classical analytical tools

The following results are standard and will be applied in later proofs. We state them for completeness.

Theorem 3.5 (Arzelà–Ascoli)**.** [37, Chapter 3]. *A uniformly bounded and equicontinuous family $\mathcal{F} \subset C([a, b])$ is relatively compact.*

Theorem 3.6 (Schauder fixed-point theorem [37, Chapter 3])**.** *Let K be a nonempty, convex, compact subset of a Banach space, and $T : K \to K$ be continuous. Then T has at least one fixed point.*

Theorem 3.7 (Hopf bifurcation for delay differential equations)**.** [36, Chapter 11, Section 11.1] and [38, Chapter 4]. *Let the characteristic equation of a DDE admit simple roots $\lambda = \pm i\omega$ at $\tau = \tau_0$. If the transversality condition $\Re\left(\frac{d\lambda}{d\tau}\right)\Big|_{\tau=\tau_0} \neq 0$ holds, then a Hopf bifurcation occurs at τ_0, producing periodic solutions.*

The results are classical and can be found in standard references on functional and delay differential equations.

3.2. Theoretical analysis under null, constant, and periodic exposure regimes

In this section, we provide the full analytical foundation for the delayed viral–immune system. We begin with the null exposure case, establishing equilibrium existence, local stability, and delay–induced Hopf bifurcation. Thereafter, we analyze constant exposure, proving uniqueness of the endemic equilibrium, sensitivity with respect to the exposure level, and characterizing the corresponding Hopf bifurcation thresholds. Finally, we consider periodic exposure and prove the existence of T–periodic solutions via a Poincaré operator and Schauder's fixed–point theorem, followed by a Lyapunov–Krasovskii stability criterion.

Throughout this section, we denote the equilibrium concentration as C^*. When analyzing the constant exposure case, we explicitly write $C^*(C_0)$ to emphasize its dependence on the exposure level C_0. The general continuous exposure function is denoted $C_a(t)$.

Notation.
τ_k denotes the delay values at which purely imaginary roots occur, and $C_a(t)$ denotes the external exposure profile (constant, null, or periodic). We write $C^*(C_0)$ when emphasizing dependence on the constant exposure level.

Linearization notation.
Throughout the paper, the linearized coefficients are defined by

$$a = r(1 - 2C^*) - \gamma f(C^*), \qquad b = -\gamma C^* f'(C^*),$$

unless otherwise specified.

3.2.1. Functional setting and invariance

The functional framework ensuring well-posedness and biological relevance of system (3.1) is established below.

The delayed viral–immune system is analyzed:

$$\frac{dC(t)}{dt} = r\,C(t)(1 - C(t)) - \gamma\,C(t)\,f(C(t-\tau)) + \rho\,C_a(t), \tag{3.1}$$

under three exposure regimes: (i) null exposure $C_a = 0$, (ii) constant exposure $C_a = C_0 > 0$, and (iii) periodic exposure $C_a(t + T) = C_a(t)$. Our assumptions are consistent with classical within–host

viral dynamics and immune interaction models [**?**, 1, 2], as well as standard delay differential equation frameworks [35, 36, 38].

The following assumptions specify the structural properties of the immune response and the interaction terms, ensuring well-posedness, positivity, and biological consistency of the model.

Let $\mathcal{X} = C([-\tau, 0], \mathbb{R})$ and define

$$\mathcal{X}_+ = \{\phi \in \mathcal{X} : 0 \le \phi(\theta) \le 1\}.$$

Assumption 2 (Immune response function)**.** The function

$$f : \mathbb{R}_{\ge 0} \to \mathbb{R}_{\ge 0}$$

satisfies the following properties:

(1) f is continuous and locally Lipschitz continuous.
(2) f is non-decreasing and bounded, with

$$0 \le f(C) \le f_{\max}, \quad \forall\, C \ge 0.$$

(3) $f(0) = 0$, and f is continuously differentiable on the interval $(0, 1)$.

Assumption 3 (Balance between exposure and immune response)**.** The model parameters satisfy

$$\gamma f(1) \ge \sup_{t \ge 0} \rho C_a(t).$$

Assumption 4 (Monotonicity condition)**.** The function

$$h(C) = \gamma C f(C) - rC(1 - C)$$

is strictly increasing in a neighborhood of the equilibrium C^*.

Remark 3.8. A sufficient condition for Assumption 4 is

$$\gamma(f(C) + Cf'(C)) > r(1 - 2C), \quad \forall C \in (0, 1).$$

Proposition 3.9 (Positivity and invariance [35])**.** *Under Assumptions 2–3, the set $\mathcal{X}_+$ is positively invariant under the semiflow associated with* (3.1).

Proof. [Sketch of proof] To establish the positive invariance of $\mathcal{X}_+$, we examine the behavior of the vector field on the boundaries of the interval $[0, 1]$. At $C = 0$, system (3.1) reduces to $\dot{C}(t) = \rho C_a(t) \ge 0$, which guarantees non-negativity of solutions. At the upper boundary $C = 1$, the derivative satisfies:

$$\dot{C}(t) = \rho C_a(t) - \gamma f(C(t - \tau)).$$

Since f is non-decreasing and $C(t - \tau) \le 1$ for t near the boundary, we have $f(C(t - \tau)) \le f(1)$. It follows from Assumption 3 that

$$\dot{C}(t) \le \rho C_a(t) - \gamma f(1) \le 0.$$

Because the vector field points inward (or is tangent) at $C = 0$ and $C = 1$, any solution $C(t)$ with initial history $\phi \in \mathcal{X}_+$ is confined to $[0, 1]$ for all $t \ge 0$.

Remark 3.10 (Order preservation and monotonicity). Consider scalar delay differential equations of the form

$$\dot{C}(t) = F(C(t), C(t-\tau)).$$

The semiflow generated by such equations is *order-preserving* provided that $\frac{\partial F}{\partial C(t-\tau)} \leq 0$. In system (3.1), the delayed term $-\gamma C f(C(t-\tau))$ satisfies this requirement since f is non-decreasing. As a result, if two initial histories satisfy $\phi_1(\theta) \leq \phi_2(\theta)$ for all $\theta \in [-\tau, 0]$, then their corresponding solutions obey

$$C(t, \phi_1) \leq C(t, \phi_2), \quad \forall\, t \geq 0.$$

3.2.2. Case I: Null exposure ($C_a = 0$)

Under null exposure, system (3.1) reduces to

$$\frac{dC}{dt} = rC(1-C) - \gamma C f(C(t-\tau)), \tag{3.2}$$

where $C(t)$ is the concentration of an immune effector.

Equilibria

Equilibria C^* satisfy

$$rC^*(1-C^*) = \gamma C^* f(C^*), \tag{3.3}$$

which can be rewritten as $g(C^*) = 0$ with

$$g(C) = rC(1-C) - \gamma C f(C).$$

Theorem 3.11 (Existence of equilibria)**.** *Under Assumption 2, system* (3.2) *admits:*

(1) *trivial equilibrium* $C^* = 0$.
(2) *least one positive equilibrium* $C^* \in (0, 1)$.

Proof. [Sketch of proof] The equilibria of (3.2) are the solutions to $C[r(1-C) - \gamma f(C)] = 0$, which immediately yields the trivial equilibrium $C^* = 0$. For $C \in (0, 1)$, we define the continuous auxiliary function:

$$g(C) = r(1-C) - \gamma f(C).$$

Given the assumptions $f(0) = 0$ and $f(1) > 0$, we observe that $g(0) = r > 0$ and $g(1) = -\gamma f(1) < 0$. By the Intermediate Value Theorem, there exists at least one $C^* \in (0, 1)$ such that $g(C^*) = 0$, confirming the existence of a positive equilibrium.

Remark 3.12 (Biological plausibility of $f(1) > 0$). The assumption $f(1) > 0$ implies that at maximum normalized viral carrying capacity ($C = 1$), the immune system mounts a non-zero response. An entirely absent immune response at peak infection ($f(1) = 0$) is biologically unrealistic for an immunocompetent host.

Local stability of equilibria

Let $x(t) = C(t) - C^*$. Linearizing around C^* yields

$$\dot{x}(t) = ax(t) + bx(t-\tau),$$

with

$$a = r(1-2C^*) - \gamma f(C^*), \qquad b = -\gamma C^* f'(C^*).$$

The characteristic equation associated with the linear system is

$$\lambda - a - be^{-\lambda\tau} = 0.$$

Theorem 3.13 (Local stability and Hopf bifurcation)**.** *Under Assumption 2:*

(1) *If $\tau = 0$, then the equilibrium C^* is asymptotically stable if and only if $a + b < 0$.*
(2) *If $\tau > 0$, then a Hopf bifurcation occurs at parameters where $b^2 > a^2$.*

Proof. [Sketch of proof] The characteristic equation for the linearized system is

$$\lambda - a - be^{-\lambda\tau} = 0. \tag{3.4}$$

For $\tau = 0$, the unique eigenvalue is $\lambda = a + b$, implying the equilibrium is asymptotically stable if and only if $a + b < 0$.

For $\tau > 0$, instability arises if roots cross the imaginary axis. Substituting $\lambda = i\omega$ ($\omega > 0$) into (3.4) and separating the real and imaginary parts yields:

$$a + b\cos(\omega\tau) = 0,$$
$$\omega - b\sin(\omega\tau) = 0.$$

Squaring and summing these equations gives $\omega^2 = b^2 - a^2$. Hence, a real, positive root $\omega = \sqrt{b^2 - a^2}$ exists if and only if $b^2 > a^2$. The corresponding critical delays are:

$$\tau_k = \frac{1}{\omega}\left[\arccos\left(-\frac{a}{b}\right) + 2k\pi\right], \quad k \in \mathbb{N}_0.$$

To confirm the Hopf bifurcation, we verify the transversality condition. Implicit differentiation of (3.4) with respect to τ evaluated at $\lambda = i\omega$ gives:

$$\Re\left(\left.\frac{d\lambda}{d\tau}\right|_{\tau=\tau_k}\right) = \frac{b\omega\sin(\omega\tau_k)}{|1 + b\tau_k e^{-i\omega\tau_k}|^2}.$$

Since $\sin(\omega\tau_k) = \omega/b \neq 0$ and $\omega > 0$, it follows that $\Re\left(\frac{d\lambda}{d\tau}\right) \neq 0$. This non-zero real part guarantees a transversal crossing of the imaginary axis, establishing the Hopf bifurcation at each critical delay τ_k.

Biologically, the emergence of a Hopf bifurcation indicates that delayed immune activation may destabilize steady viral control and induce sustained oscillations in viral load. This suggests that sufficiently long immune delays may lead to recurrent viral rebounds, a phenomenon consistent with observed fluctuations in infections where immune response timing is impaired.

Global stability via the Lyapunov–Razumikhin method

We establish global asymptotic stability of the positive equilibrium C^* in the absence of external exposure ($C_a \equiv 0$).

Theorem 3.14 (Global asymptotic stability)**.** *Suppose Assumption 2 holds, then let $C^* \in (0,1)$ be the equilibrium of* (3.2)*. Assume that there exists $\alpha > 0$ such that*

$$(C - C^*)[g(C) - g(C^*)] \leq -\alpha(C - C^*)^2$$

for all C in a neighborhood of C^*, and that f is Lipschitz continuous on $[0,1]$ *with Lipschitz constant L. If there exists a constant $q > 1$ such that*

$$\alpha > \gamma L\,(1 + \sqrt{q})\,, \tag{3.5}$$

then the equilibrium C^* of (3.2) *is globally asymptotically stable for all $\tau \geq 0$.*

Proof. Let $C^* \in (0,1)$ be the positive equilibrium. Define the quadratic Lyapunov function:

$$V(C(t)) = \frac{1}{2}(C(t) - C^*)^2.$$

Function V satisfies the bounding condition $c_1|C - C^*|^2 \leq V(C) \leq c_2|C - C^*|^2$ with $c_1 = c_2 = \frac{1}{2}$.

Differentiating V along the solutions of (3.2) yields:

$$\begin{aligned}\dot{V}(t) &= (C(t) - C^*)\left[rC(t)(1 - C(t)) - \gamma C(t) f(C(t-\tau))\right] \\ &= (C(t) - C^*)\left[g(C(t)) + \gamma C(t) f(C(t)) - \gamma C(t) f(C(t-\tau))\right],\end{aligned}$$

where $g(C) = rC(1 - C) - \gamma C f(C)$. Since $g(C^*) = 0$, we can rewrite the derivative as:

$$\dot{V}(t) = (C(t) - C^*)[g(C(t)) - g(C^*)] + \gamma C(t)(C(t) - C^*)[f(C(t)) - f(C(t-\tau))]. \tag{3.6}$$

By the assumed local dissipativity condition at C^*, the instantaneous term satisfies:

$$(C(t) - C^*)[g(C(t)) - g(C^*)] \leq -\alpha(C(t) - C^*)^2.$$

To bound the delayed term, we impose the Razumikhin condition. Assume there exists $q > 1$ such that $V(C(t+\theta)) \leq qV(C(t))$ for all $\theta \in [-\tau, 0]$. This implies:

$$\frac{1}{2}(C(t-\tau) - C^*)^2 \leq q\frac{1}{2}(C(t) - C^*)^2 \implies |C(t-\tau) - C^*| \leq \sqrt{q}|C(t) - C^*|.$$

Using the triangle inequality, the difference in the state variables is bounded by:

$$|C(t) - C(t-\tau)| \leq |C(t) - C^*| + |C^* - C(t-\tau)| \leq (1 + \sqrt{q})|C(t) - C^*|.$$

Applying the Lipschitz continuity of f and the invariant bound $C(t) \leq 1$ (Lemma 3.3), the cross term in (3.6) satisfies:

$$\gamma C(t)|C(t) - C^*||f(C(t)) - f(C(t-\tau))| \le \gamma \cdot 1 \cdot |C(t) - C^*| \cdot L|C(t) - C(t-\tau)|$$
$$\le \gamma L(1 + \sqrt{q})(C(t) - C^*)^2.$$

Substituting these bounds into (3.6) yields:

$$\dot{V}(t) \le -\left[\alpha - \gamma L(1 + \sqrt{q})\right](C(t) - C^*)^2.$$

Under condition (3.5), we define $c_3 = \alpha - \gamma L(1 + \sqrt{q}) > 0$, ensuring $\dot{V}(t) \le -c_3(C(t) - C^*)^2$. By Theorem 3.4, the positive equilibrium C^* is globally asymptotically stable.

From a biological perspective, this result indicates that when the immediate immune response dominates delayed effects, the system maintains stable viral control regardless of the activation delay.

In the absence of external exposure ($C_a = 0$), the system dynamics are governed by the interplay between intrinsic replication and delayed immune feedback. The model admits a biologically meaningful positive equilibrium C^*. The above result shows that if the instantaneous stabilizing effect dominates the delayed immune response, then the equilibrium remains globally stable independently of the delay.

3.2.3. Case II: Constant exposure ($C_a = C_0 > 0$)

In the presence of a constant external viral source, the within-host viral dynamics are governed by

$$\frac{dC}{dt} = rC(1 - C) - \gamma C f(C(t-\tau)) + \rho C_0, \tag{3.7}$$

where ρC_0 represents a constant influx of virus.

Equilibria and uniqueness

The steady states C^* of (3.7) satisfy

$$\Phi(C) := \gamma C f(C) - rC(1 - C) - \rho C_0 = 0. \tag{3.8}$$

Theorem 3.15 (Existence and uniqueness)**.** *Under Assumptions 2 and 4, if the constant exposure satisfies*

$$\rho C_0 < \gamma f(1), \tag{3.9}$$

then Eq (3.8) *admits a unique solution* $C^*(C_0) \in (0, 1)$*, which defines the unique positive equilibrium of* (3.7)*.*

Proof. Consider the mapping $\Phi : [0, 1] \to \mathbb{R}$ defined in (3.8). Since $f \in C^1([0, 1])$, it follows that $\Phi \in C^1([0, 1])$, hence Φ is continuous on $[0, 1]$.

Evaluating the mapping at the endpoints:

$$\Phi(0) = -\rho C_0 < 0, \qquad \Phi(1) = \gamma f(1) - \rho C_0 > 0,$$

where the last inequality follows from the hypothesis $\rho C_0 < \gamma f(1)$. By the Intermediate Value Theorem, there exists at least one $C^* \in (0,1)$ such that $\Phi(C^*) = 0$.

Differentiating Φ yields

$$\Phi'(C) = \gamma\left(f(C) + Cf'(C)\right) - r(1-2C).$$

By Assumption 4, we have $\Phi'(C) > 0$ for all $C \in (0,1)$. Hence, Φ is strictly increasing on $(0,1)$ and continuous on $[0,1]$. Therefore, Φ admits at most one zero in $(0,1)$. Combined with the existence result, this proves that equilibrium C^* is unique.

Remark 3.16 (Biological feasibility and limiting behavior). Condition $\rho C_0 < \gamma f(1)$ ensures that the constant viral influx does not exceed the maximal immune clearance capacity at $C = 1$. We note that in the limiting case $\rho C_0 \to 0$, the equation reduces to the equilibrium condition of the null-exposure case, recovering the structure analyzed in Section 3.1.

Remark 3.17 (Prevention of bistability). Assumption 4 is a standard criterion in population dynamics and immunology to avoid multiple positive equilibria or subcritical transitions.

Remark 3.18 (Connection to stability analysis). While Theorem 3.15 guarantees the unique positive equilibrium, the stability of this equilibrium under time delay $\tau > 0$ can be analyzed using a Razumikhin-type argument similar to Section 3.1. Under suitable conditions ensuring that the instantaneous feedback dominates the delayed immune response (analogous to condition (3.5)), one obtains global asymptotic stability for sufficiently small delays τ.

Dependence on exposure level

We analyze the sensitivity of the positive equilibrium $C^*(C_0)$ with respect to the constant exposure level $C_0 > 0$. Let $C^*(C_0) \in (0,1)$ denote the unique equilibrium given by Theorem 3.15. Define the mapping $F : (0,1) \times \mathbb{R}^+ \to \mathbb{R}$ by

$$F(C, C_0) := rC(1-C) - \gamma C f(C) + \rho C_0. \tag{3.10}$$

The equilibrium is characterized implicitly by

$$F(C^*(C_0), C_0) = 0.$$

Proposition 3.19 (Sensitivity of the equilibrium)**.** *Assume that f is continuously differentiable on $(0,1)$. If*

$$\frac{\partial F}{\partial C}(C^*, C_0) \neq 0,$$

then the mapping $C_0 \mapsto C^*(C_0)$ is continuously differentiable in a neighborhood of C_0, and its derivative is given by

$$\frac{dC^*}{dC_0} = \frac{\rho}{\gamma(f(C^*) + C^* f'(C^*)) - r(1-2C^*)}. \tag{3.11}$$

Proof. Since f is C^1 on $(0,1)$, the function F defined in (3.10) is continuously differentiable on $(0,1) \times \mathbb{R}^+$. Its partial derivatives are

$$\frac{\partial F}{\partial C} = r(1-2C) - \gamma(f(C) + Cf'(C)), \tag{3.12}$$

$$\frac{\partial F}{\partial C_0} = \rho. \tag{3.13}$$

Since $F(C, C_0)$ is C^1 on $(0,1) \times \mathbb{R}_{\geq 0}$ and $\frac{\partial F}{\partial C}(C^*, C_0) \neq 0$ by Assumption 4, the Implicit Function Theorem ensures the existence of an open interval I containing C_0 and a unique C^1 function $C^*(\cdot) : I \to (0,1)$ such that

$$F(C^*(C_0), C_0) = 0, \quad \forall\, C_0 \in I.$$

Moreover, C^* is differentiable with respect to C_0, and its derivative satisfies

$$\frac{dC^*}{dC_0} = -\frac{\frac{\partial F}{\partial C_0}}{\frac{\partial F}{\partial C}}.$$

Substituting (3.12)–(3.13) yields

$$\frac{dC^*}{dC_0} = -\frac{\rho}{r(1-2C^*) - \gamma\big(f(C^*) + C^* f'(C^*)\big)},$$

which is equivalent to (3.11).

Corollary 3.20 (Monotonicity with respect to exposure)**.** *Under Assumption 4, the unique positive equilibrium satisfies*

$$\frac{dC^*}{dC_0} > 0. \tag{3.14}$$

Thus, the equilibrium viral concentration is a strictly increasing function of the exposure level C_0.

Proof. From (3.11), we have

$$\frac{dC^*}{dC_0} = \frac{\rho}{\gamma\big(f(C^*) + C^* f'(C^*)\big) - r(1-2C^*)}.$$

Since $\rho > 0$, the sign of $\frac{dC^*}{dC_0}$ is determined by the denominator. Under Assumption 4, the denominator is strictly positive at $C = C^*$, and therefore $\frac{dC^*}{dC_0} > 0$.

Remark 3.21 (Stability and Critical Transitions). The denominator in (3.11) coincides with $\Phi'(C^*)$, where Φ is defined in (3.8). Therefore, the sensitivity of the equilibrium is directly linked to its local stability properties. In particular:

- As $\Phi'(C^*) \to 0$, the derivative $\frac{dC^*}{dC_0}$ becomes unbounded. This reflects a loss of normal hyperbolicity and signals the onset of a critical transition, typically associated with a saddle-node bifurcation in the parameter C_0.
- In the limiting case $\rho C_0 \to 0$, Eq (3.11) reduces to the sensitivity structure of the null-exposure regime, consistently recovering the framework of Section 3.1.

Remark 3.22 (Biological Interpretation). Condition $\frac{dC^*}{dC_0} > 0$ confirms that sustained external exposure increases the steady-state viral load. The magnitude of this sensitivity is modulated by the immune response:

- Strong Immune Feedback: Large values of $f'(C^*)$ or a high clearance rate γ increase the denominator in (3.11), thereby reducing $\frac{dC^*}{dC_0}$ and buffering the effect of exposure.
- Immune Saturation: If the immune response saturates (i.e., $f'(C^*) \to 0$), the denominator decreases, leading to high sensitivity. In this regime, even small increases in exposure can significantly elevate the equilibrium viral load.

Hopf bifurcation with constant exposure

We analyze the emergence of oscillatory dynamics in system (3.7) under constant exposure $C_a = C_0 > 0$. Let $C^* = C^*(C_0) \in (0, 1)$ denote the unique positive equilibrium established in Theorem 3.15. Linearizing system (3.7) around C^* yields the delay differential equation

$$\dot{x}(t) = ax(t) + bx(t - \tau), \tag{3.15}$$

where the coefficients are defined as

$$a = r(1 - 2C^*) - \gamma f(C^*), \qquad b = -\gamma C^* f'(C^*).$$

The associated characteristic equation is given by

$$\lambda - a - be^{-\lambda\tau} = 0. \tag{3.16}$$

The following analysis characterizes the destabilization of C^* through delay-induced oscillations [36, 38].

Theorem 3.23 (Hopf bifurcation under constant exposure)**.** *Assume that $b^2 > a^2$. Then there exists a sequence of critical delays $\{\tau_k\}_{k\in\mathbb{N}}$ such that the characteristic equation* (3.16) *admits a pair of simple purely imaginary roots $\lambda = \pm i\omega$ at $\tau = \tau_k$, where*

$$\omega = \sqrt{b^2 - a^2}. \tag{3.17}$$

The critical delays are defined by

$$\tau_k = \frac{1}{\omega}\left(\arccos\left(-\frac{a}{b}\right) + 2k\pi\right), \quad k \in \mathbb{N}. \tag{3.18}$$

Moreover, the transversality condition holds, and the system undergoes a Hopf bifurcation at each τ_k, giving rise to periodic solutions bifurcating from equilibrium C^*.

Proof. We seek purely imaginary roots $\lambda = i\omega$ ($\omega > 0$) of (3.16). Substituting $\lambda = i\omega$ into the characteristic equation and applying Euler's formula yields

$$i\omega - a - b(\cos(\omega\tau) - i\sin(\omega\tau)) = 0.$$

Separating the real and imaginary parts, we obtain the system:

$$a + b\cos(\omega\tau) = 0, \tag{3.19}$$

$$\omega - b\sin(\omega\tau) = 0. \tag{3.20}$$

Squaring and summing (3.19) and (3.20) lead to $a^2 + \omega^2 = b^2$. This yields $\omega = \sqrt{b^2 - a^2}$. Hence, purely imaginary roots exist if and only if $b^2 > a^2$, in which case $\omega > 0$ is well defined. Moreover, the condition $|\frac{a}{b}| < 1$ ensures that Eq (3.19) admits solutions for τ, yielding the sequence of critical delays τ_k in (3.18).

We now verify the simplicity of the roots and the transversality condition. The roots $\lambda = \pm i\omega$ are simple because

$$\frac{\partial}{\partial\lambda}(\lambda - a - be^{-\lambda\tau}) = 1 + b\tau e^{-\lambda\tau} \neq 0 \quad \text{at } \lambda = i\omega,$$

which holds since $b^2 > a^2$ ensures $\omega \neq 0$.

Differentiating the characteristic equation (3.16) implicitly with respect to τ gives

$$\frac{d\lambda}{d\tau} = -\frac{b\lambda e^{-\lambda\tau}}{1 + b\tau e^{-\lambda\tau}}.$$

Evaluating at $\lambda = i\omega$ and $\tau = \tau_k$, we find

$$\Re\left(\frac{d\lambda}{d\tau}\right) = -\frac{b\omega \sin(\omega\tau_k)}{|1 + b\tau_k e^{-i\omega\tau_k}|^2} \neq 0,$$

because $\omega > 0$, $b \neq 0$, and $\sin(\omega\tau_k) \neq 0$ (equivalently, $\sqrt{b^2 - a^2} \neq 0$).

Hence, the transversality condition holds, and the eigenvalues cross the imaginary axis with nonzero speed. By the Hopf bifurcation theorem for delay differential equations [36, 38], a family of periodic solutions bifurcates from C^* at each τ_k.

Remark 3.24 (Biological interpretation of the bifurcation condition). Condition $b^2 > a^2$ is equivalent to

$$\gamma C^* f'(C^*) > |r(1 - 2C^*) - \gamma f(C^*)|.$$

Biologically, this represents a regime where immune sensitivity is high relative to the net viral growth at equilibrium. In such scenarios, the immune system reacts strongly to viral fluctuations, but the feedback delay τ causes the response to be out of phase with the current viral load, leading to sustained clinical flare-ups.

Remark 3.25. As the delay τ increases, the system may undergo successive Hopf bifurcations at τ_k, leading to increasingly complex oscillatory dynamics or the coexistence of periodic orbits.

3.2.4. Case III: Periodic exposure ($C_a(t + T) = C_a(t)$)

In this section, we investigate the dynamics of the system under a non-constant, periodic environmental stimulus. We consider the periodically forced delay differential equation (DDE):

$$\frac{dC(t)}{dt} = rC(t)(1 - C(t)) - \gamma C(t) f(C(t - \tau)) + \rho C_a(t), \tag{3.21}$$

where the external exposure $C_a : \mathbb{R}_+ \to \mathbb{R}_+$ is a continuous, T-periodic function. A biologically relevant example, representing daily or cyclic variations, is the sinusoidal variation:

$$C_a(t) = C_0\Big(1 + \eta \sin(\omega t)\Big), \quad T = \frac{2\pi}{\omega}, \tag{3.22}$$

with $0 \leq \eta < 1$ ensuring the non-negativity of the viral intake.

Existence of a periodic solution

Theorem 3.26 (Existence of T–periodic solution)**.** *Under Assumptions 2 and 3, system* (3.21) *admits at least one T–periodic solution $C^*(t)$ such that $0 < C^*(t) \leq 1$ for all $t \in [0, T]$.*

Proof. [Sketch of proof of Theorem 3.26] Let $\mathcal{X} = C([-\tau, 0], \mathbb{R})$ be the Banach space of continuous functions with the supremum norm. Define the convex, closed set

$$K = \{\phi \in \mathcal{X} : 0 \le \phi(\theta) \le 1,\ \forall \theta \in [-\tau, 0]\}. \tag{3.23}$$

Let $C(t; \phi)$ denote the unique solution of (3.21) with initial history $\phi \in K$.

By Proposition 3.9, K is forward-invariant. Specifically:

- At the upper boundary $C = 1$: Assumption 3 ensures
$$\dot{C} = rC(1 - C) - \gamma C f(C(t - \tau)) + \rho C_a(t) \le 0.$$
- At the lower boundary $C = 0$: $\dot{C} = \rho C_a(t) \ge 0$, and since $C_a(t) \not\equiv 0$, positivity is maintained for $t > 0$.

Define the Poincaré operator $\mathcal{P} : K \to K$ by

$$(\mathcal{P}\phi)(\theta) = C(T + \theta; \phi), \quad \theta \in [-\tau, 0].$$

Continuous dependence on initial data ensures $\mathcal{P}$ is continuous.

Since f and C_a are continuous on bounded sets, the derivative $\dot{C}(t; \phi)$ is uniformly bounded for all $\phi \in K$. Hence, the family $\{C(\cdot; \phi) : \phi \in K\}$ is equicontinuous and uniformly bounded on $[0, T]$. By the Arzelà–Ascoli theorem, $\mathcal{P}(K)$ is relatively compact in $\mathcal{X}$.

Moreover, since the solution map $T(t) : \mathcal{X} \to \mathcal{X}$ is continuous and compact on K, it follows that the Poincaré operator

$$\mathcal{P} : \phi \mapsto T(T)\phi$$

is completely continuous on K.

$\mathcal{P}$ is completely continuous and maps the non-empty, closed, convex set K into itself. By Schauder's fixed-point theorem [39], there exists $\phi^* \in K$ such that

$$\mathcal{P}(\phi^*) = \phi^*.$$

The corresponding solution $C^*(t)$ with initial history ϕ^* satisfies $C^*(t + T) = C^*(t)$ and is therefore T-periodic.

Remark 3.27 (Biological synchronization). Theorem 3.26 confirms that the viral load $C(t)$ can entrain to the frequency of environmental exposure.

Perturbative approximation for small forcing When the forcing amplitude is small ($C_0 \ll 1$), the system can be analyzed as a perturbation around the constant-exposure equilibrium C_0^*. Define

$$C(t) = C_0^* + \eta(t), \quad |\eta(t)| \ll C_0^*, \tag{3.24}$$

and assume f is C^1 at C_0^*. Linearizing (3.21) gives the non-homogeneous linear delay differential equation

$$\dot{\eta}(t) = a\eta(t) + b\eta(t - \tau) + \rho\delta C_a(t), \tag{3.25}$$

with

$$a = r(1 - 2C_0^*) - \gamma f(C_0^*), \quad b = -\gamma C_0^* f'(C_0^*), \quad \delta C_a(t) = \frac{1}{2} C_0 \sin(\omega t).$$

Proposition 3.28 (Steady-state response to small periodic forcing)**.** *Let $\eta(t)$ satisfy* (3.25)*. Then the steady-state amplitude of oscillation is approximated by*

$$\eta_{\max} \approx \frac{\rho C_0/2}{\sqrt{(a + b\cos(\omega\tau))^2 + (\omega - b\sin(\omega\tau))^2}}. \tag{3.26}$$

Proof. [Sketch of proof] Equation (3.25) is linear and driven by a sinusoidal input. The characteristic operator is

$$D(s) = s - a - be^{-s\tau}.$$

Assuming a solution of the form $\eta(t) = \eta_0 e^{i\omega t}$, substitution yields

$$i\omega\eta_0 = a\eta_0 + b\eta_0 e^{-i\omega\tau} + \rho C_0/2 \implies \eta_0 = \frac{\rho C_0/2}{i\omega - a - be^{-i\omega\tau}}.$$

Taking the modulus gives the amplitude estimate (3.26). The approximation neglects higher-order nonlinear terms $O(\eta^2)$ and is valid for sufficiently small C_0.

Remark 3.29 (Biological interpretation). Small-amplitude forcing induces harmonic oscillations around C_0^*, representing the immune system tracking environmental cycles. Resonance occurs when the forcing frequency ω approaches the system's intrinsic frequency (Hopf bifurcation), leading to amplified viral load oscillations. For larger C_0, nonlinear effects may lead to multi-stability or complex dynamics.

Floquet and Lyapunov–Krasovskii stability The stability of the T-periodic solution $C^*(t)$ of (3.21) is analyzed via the linear variational equation

$$\dot{\xi}(t) = A(t)\xi(t) + B(t)\xi(t - \tau), \tag{3.27}$$

where the T-periodic coefficients are

$$A(t) = r(1 - 2C^*(t)) - \gamma f(C^*(t - \tau)), \quad B(t) = -\gamma C^*(t) f'(C^*(t - \tau)).$$

Let $\Phi(t)$ denote the evolution operator associated with the variational equation (3.27) on the state space $\mathcal{X} = C([-\tau, 0], \mathbb{R})$. The monodromy operator is defined by

$$\mathcal{M} := \Phi(T) : \mathcal{X} \to \mathcal{X},$$

whose spectrum consists of the Floquet multipliers $\{\mu_k\}$. Local exponential stability of the periodic solution is equivalent to

$$\max_k |\mu_k| < 1.$$

Proposition 3.30 (Local stability of the periodic orbit)**.** *Let $C^*(t)$ be a T-periodic solution of* (3.21)*. Then $C^*(t)$ is locally asymptotically stable if either of the following conditions holds:*

(1) *Floquet condition: All Floquet multipliers μ of the monodromy operator $\mathcal{M}$ satisfy*

$$|\mu| < 1.$$

(2) *Lyapunov–Krasovskii condition: There exists a T-periodic weighting function $\phi(t)$ such that*

$$\phi(t) \geq \epsilon > 0, \quad \forall t \in [0, T],$$

and

$$\phi(t) = \frac{1}{2}|B(t+\tau)| + \epsilon,$$

such that

$$A(t) + \frac{1}{2}|B(t)| + \frac{1}{2}|B(t+\tau)| < 0, \quad \forall t \in [0, T]. \tag{3.28}$$

Proof. [Sketch of proof] Equation (3.27) defines a continuous evolution operator on the Banach space $\mathcal{X} = C([-\tau, 0], \mathbb{R})$. Over one period T, the monodromy operator $\Phi(T)$ maps the initial history segment to the solution after time T. If all Floquet multipliers satisfy $|\mu| < 1$, then $\Phi(T)^n \to 0$ as $n \to \infty$, implying exponential decay of perturbations and hence local asymptotic stability.

Consider the functional

$$V(\xi_t) = \frac{1}{2}\xi^2(t) + \int_{t-\tau}^{t} \phi(s)\xi^2(s)ds.$$

Differentiating along solutions of (3.27) gives

$$\frac{d}{dt}V(\xi_t) = A(t)\xi^2(t) + B(t)\xi(t)\xi(t-\tau) + \phi(t)\xi^2(t) - \phi(t-\tau)\xi^2(t-\tau).$$

Using the inequality $|\xi(t)\xi(t-\tau)| \leq \frac{1}{2}(\xi^2(t) + \xi^2(t-\tau))$ and the choice of $\phi(t)$ in (3.28) yields

$$\frac{d}{dt}V(\xi_t) \leq \Big(A(t) + \frac{1}{2}|B(t)| + \frac{1}{2}|B(t+\tau)|\Big)\xi^2(t) < 0, \quad \forall t,$$

which guarantees asymptotic decay of perturbations. This establishes local stability under the Lyapunov–Krasovskii criterion.

Remark 3.31 (Small-delay approximation). For sufficiently small τ, the delay term is a perturbation, and stability can be approximated by the averaged scalar condition

$$\int_0^T A(s)\, ds < 0.$$

3.3. Analytical interpretation of numerical regimes

The analytical results obtained under null, constant, and periodic exposure provide a structural foundation for interpreting the numerical regimes identified in Section 5. Although not all exposure profiles investigated numerically admit a closed-form analytical treatment, the qualitative behavior observed across the sixteen simulated scenarios is governed by the same delayed feedback mechanisms characterized in the theoretical analysis.

In particular, linearization of the delayed system around a steady state leads to the characteristic equation

$$\lambda - a - b\, \mathrm{e}^{-\lambda\tau} = 0, \tag{3.29}$$

where the coefficients

$$a = r(1 - 2C^*) - \gamma f(C^*), \qquad b = -\gamma C^* f'(C^*)$$

encode the balance between intrinsic viral growth and immune feedback. The analytical condition $b^2 > a^2$, which signals the onset of Hopf bifurcation, corresponds numerically to regimes displaying sustained oscillations, nonzero asymptotic amplitude, and local maxima. These features are observed under periodic exposure for highly nonlinear immune responses, as quantified by the asymptotic amplitude and the number of peaks (Figures 7 and 8).

Conversely, the delay-independent stability criterion $|b| < -a$ explains the numerically observed exponential convergence toward steady states. In such regimes, the post-peak decay rate λ_{decay} is strictly positive and well fitted by an exponential model, a signature of stable dynamics. This behavior is consistently observed for linear and Michaelis–Menten immune responses under constant and adaptive exposure, confirming the predictive power of the analytical stability conditions.

While event-driven and adaptive exposure profiles are not treated explicitly in the theoretical framework, they can be interpreted as non-autonomous perturbations of the constant and periodic regimes, respectively. Their qualitative behavior remains governed by the same feedback coefficients a and b, which explains the robustness of the numerical ordering across metrics such as peak viral load, cumulative burden, terminal viral load, and relative clearance time. In particular, impulsive exposure excites transient dynamics whose decay rate is controlled by the same delayed immune feedback identified analytically, leading either to rapid clearance or to prolonged oscillatory relaxation.

Overall, the theoretical analysis provides a coherent explanation for the numerically observed transitions between stable equilibria, entrained oscillations, and non-convergent transient dynamics.

4. Numerical methodology and metrics

In this section, we describe the numerical framework used to explore the delayed viral–immune system introduced in Section 3.2, together with the quantitative metrics employed to compare dynamical behaviors across immune response architectures and exposure profiles.

4.1. Numerical integration of the delayed system

The delayed differential equation (2.1) is solved numerically using a method-of-steps approach with explicit time integration. The delayed term $C(t - \tau)$ is evaluated by linear interpolation of previously computed solution values when required.

Time discretization and numerical scheme. The equation is discretized on a uniform time grid

$$t_n = n\,\Delta t, \quad n = 0, 1, \ldots, N.$$

An explicit forward Euler scheme is used:

$$C_{n+1} = C_n + \Delta t\left[rC_n(1 - C_n) - \gamma C_n f(C_{n-\ell}) + \rho C_a(t_n)\right],$$

where the delay index is defined by

$$\ell = \left\lfloor \frac{\tau}{\Delta t} \right\rfloor.$$

Index ℓ represents the number of time steps corresponding to the delay τ, thereby enabling evaluation of the delayed term within the discrete scheme.

The scheme is first-order accurate in time and requires sufficiently small Δt to ensure numerical stability.

When τ is not an integer multiple of Δt, the delayed term is approximated by linear interpolation:

$$C(t_n - \tau) \approx (1 - \theta)C_{n-\ell-1} + \theta C_{n-\ell}, \quad \theta = \frac{\tau - \ell\Delta t}{\Delta t}.$$

All simulations are initialized with a constant history function

$$C(t) \equiv C_0 \quad \text{for } t \in [-\tau, 0],$$

with $C_0 > 0$ sufficiently small to represent an initial infection. The time step is fixed to $\Delta t = 0.01$, and the simulation horizon T_{sim} is chosen large enough to eliminate transient dynamics and capture long-term behavior, including convergence or persistent oscillations.

For reproducibility, the explicit normalized expressions of the exposure and immune response functions used in simulations are provided in Appendix (Tables A1 and A2).

4.2. Baseline parameter values

Unless otherwise specified, all simulations are conducted using the baseline parameter set reported in Table 3. These values are chosen to reproduce the characteristic kinetics of acute respiratory viral infections, including influenza A and SARS-CoV-2.

The intrinsic viral replication rate r and immune clearance rate γ are calibrated to reflect rapid within-host viral turnover and an effective immune response, consistent with empirical estimates indicating fast clearance of free viral particles (e.g., a half-life on the order of hours for influenza) [5, 24]. The external forcing intensity ρ represents a biologically plausible continuous exposure or background inoculum, as considered in transmission-coupled within-host frameworks [40].

The immune activation delay is fixed at $\tau = 2.0$ days, agreeing with reported intracellular delays and $CD8^+$ T-cell expansion times (typically 1.8–2.6 days) [41]. From a dynamical systems perspective, this choice places the system in proximity to a Hopf bifurcation threshold, thereby enabling a systematic investigation of delay-induced oscillatory regimes and limit-cycle behavior.

Although acute infections typically resolve within 7–14 days [24], the simulation horizon is extended to $T_{\text{sim}} = 100$ days.

To isolate the effect of immune response architecture from parameter scaling, all nonlinear immune functions are evaluated under a common set of reference parameters across scenarios. The Michaelis–Menten and Hill-type responses share a half-saturation constant $K = 0.5$, while the Hill function uses a cooperativity coefficient $n = 4$. The switch-like response is characterized by a steepness parameter $\kappa = 10$ and an activation threshold $C^* = 0.5$. These values place the activation regions on comparable scales and yield similar mid-range sensitivity across the formulations. Parameter magnitudes of this order are widely used in within-host models to capture ultrasensitive and threshold-like immune activation [28, 29].

All variables and parameters are expressed in consistent units. Time is measured in days, and viral load is normalized with respect to a reference carrying capacity, rendering $C(t)$ dimensionless.

Consequently, rate parameters are expressed in day^{-1}, while parameters associated with immune response functions are dimensionless.

Table 3. Baseline model parameters and numerical settings. The parameter values are selected to be consistent with biologically realistic ranges reported in the literature and to explore representative dynamical regimes.

Category	Parameter	Symbol	Value	Units	Biological rationale / indicative references
Growth	Viral replication rate	r	2.8	day^{-1}	Acute viral kinetics [24, 42]
Immune	Clearance rate	γ	0.25	day^{-1}	Effective immune-mediated clearance [24]
Immune	Half-saturation constant	K	0.5	–	Comparable activation range [28]
Immune	Hill coefficient	n	4	–	Ultrasensitive immune activation [29]
Immune	Switch steepness	κ	10	–	Sharp threshold response [29]
Immune	Activation threshold	C^*	0.5	–	Mid-range immune triggering [28]
Exposure	Forcing intensity	ρ	0.35	day^{-1}	Continuous exposure / inoculum [40]
Delay	Immune activation delay	τ	2.0	day	$CD8^+$ latency; near Hopf threshold [41]
Initial	Initial viral load	$C(0)$	0.01	–	Low-dose infection regime
Time	Final simulation time	T_{sim}	100	day	Asymptotic regime capture
	Time step	Δt	0.01	day	Numerical stability and accuracy

4.3. Factorial design of scenarios

A full factorial design is implemented by combining:

- four immune response functions $f(C)$ (linear, Michaelis–Menten, Hill-type, and switch-like), and
- four exposure profiles $C_a(t)$ (constant, periodic, event-driven, and adaptive).

This yields a total of sixteen scenarios, each defined by a unique pair (f, C_a). All scenarios are simulated using identical baseline parameter values for r, γ, τ, and ρ, ensuring that observed differences arise solely from immune architecture and exposure structure.

4.4. Quantitative metrics

To quantify the interplay between exposure structure and immune response architecture, we systematically simulate all combinations of the four exposure functions and the four immune response functions introduced in Sections 2.1 and 2.2. This full factorial design yields sixteen distinct scenarios, summarized in Table 4, and enables a comprehensive comparison of how immune mechanisms and contact patterns jointly shape within-host viral dynamics.

For each simulated trajectory $C_i(t)$ associated with scenario i, we extract a set of quantitative indicators that capture the intensity and temporal features of infection. These metrics are standard in within-host modeling and serve as interpretable proxies for infection severity, immune control efficiency, and dynamical regime classification. Below we define the core metrics used in the comparative analysis.

Peak viral load. The maximal infection intensity is measured as:

$$C_{\max}^{(i)} = \max_{t\in[0,T_{\text{sim}}]} C_i(t). \tag{4.1}$$

This peak viral load is indicative of disease severity and transmission potential.

Time to peak. The time required to reach the peak viral load is defined by:

$$t_{\max}^{(i)} = \arg\max_{t\in[0,T_{\text{sim}}]} C_i(t), \tag{4.2}$$

and reflects the speed of early viral proliferation and immune activation latency.

Response lag. To quantify the temporal delay between exposure and viral response, we define the response lag as the time shift that maximizes the cross-correlation between the exposure function $C_a(t)$ and the viral load trajectory $C_i(t)$:

$$\mathcal{L}^{(i)} = \arg\max_{\ell\in\mathbb{R}} \int_0^{T_{\text{sim}}} C_a(t)\, C_i(t+\ell)\, \mathrm{d}t. \tag{4.3}$$

This metric captures the effective temporal memory induced by delayed immune feedback.

Time to clearance. The viral clearance time is the earliest time at which the viral load remains permanently below a small detection threshold ε:

$$T_{\text{clear}}^{(i)} = \inf\{t \geq 0 \ : \ C_i(s) < \varepsilon \ \ \forall s \geq t\}. \tag{4.4}$$

It quantifies the duration of active infection and efficiency of long-term immune control.

Relative time to clearance. To quantify the rate at which the viral load decreases after the peak, we define the relative time to clearance at fraction $\rho \in (0,1)$ of the peak level as

$$T_{\text{rel}}(\rho) = \inf\{\, t \geq t_{\max} : C(t) \leq \rho\, C_{\max}\,\}.$$

If the threshold $\rho\, C_{\max}$ is not reached within the simulation window, we report the censored value

$$\widetilde{T}_{\text{rel}}(\rho) = \arg\min_{t\in[t_{\max},T]} C(t),$$

which corresponds to the time of the minimal post-peak viral load.

Cumulative viral burden. The total infection experienced over the simulation horizon is given by the area under the curve:

$$\text{AUC}^{(i)} = \int_0^{T_{\text{sim}}} C_i(t)\, \mathrm{d}t, \tag{4.5}$$

a widely used integrated measure combining intensity and duration of infection.

Asymptotic amplitude. To assess the presence of sustained oscillations caused by delayed immune feedback, we compute the peak-to-trough amplitude in the final portion of the trajectory:

$$\mathrm{Amp}^{(i)} = \max_{t\in[T_1,T_{\mathrm{sim}}]} C_i(t) - \min_{t\in[T_1,T_{\mathrm{sim}}]} C_i(t), \tag{4.6}$$

where $T_1 < T_{\mathrm{sim}}$ is chosen sufficiently large to exclude transients. A nonzero amplitude indicates delay-induced oscillations.

Final viral load. The terminal infection level at the end of the simulation is recorded as:

$$C^{(i)}_{\mathrm{final}} = C_i(T_{\mathrm{sim}}), \tag{4.7}$$

and provides a proxy for the long-term equilibrium (or persistent load) attained under each scenario.

Number of local maxima. To further characterize dynamic complexity, we count the number of local peaks in each trajectory:

$$N^{(i)}_{\mathrm{peaks}} = \mathrm{card}\left(\{t_k \in (0, T_{\mathrm{sim}}) \;\middle|\; C_i'(t_k) = 0,\ C_i''(t_k) < 0\}\right) \tag{4.8}$$

distinguishing single-peak scenarios (monotonic control) from multipeak or oscillatory regimes.

Post-peak decay rate. A central metric used to characterize long-term dynamics is the post-peak decay rate λ_{decay}, defined as the exponential rate at which the viral load converges toward its asymptotic state.

Let t_{peak} denote the time at which $C(t)$ attains its global maximum. We define the asymptotic reference state C^* as follows:

- for convergent trajectories, C^* is taken as the mean value of $C(t)$ over the final 20% of the simulation horizon;
- for oscillatory trajectories, C^* is defined as the average of the upper and lower envelopes, estimated from successive local maxima and minima in the asymptotic regime.

The post-peak decay rate is estimated from the exponential relaxation of the deviation from this asymptotic state,

$$|C(t) - C^*| \;\approx\; |C(t_{\mathrm{peak}}) - C^*| \exp(-\lambda_{\mathrm{decay}}(t - t_{\mathrm{peak}})), \qquad t > t_{\mathrm{peak}}. \tag{4.9}$$

The parameter λ_{decay} is obtained from a linear regression of $\log|C(t) - C^*|$ over a post-peak interval where the deviation exhibits an approximately exponential decay. A positive value of λ_{decay} indicates convergence toward C^* (stable dynamics), while $\lambda_{\mathrm{decay}} \approx 0$ signals persistent oscillations or non-convergent behavior.

Table 4. Combinations of immune response functions $f(C)$ and exposure profiles $C_a(t)$ defining the sixteen simulated scenarios.

Immune response $f(C)$	Constant	Periodic	Event-driven	Adaptive
Linear ($f(C) = C$)	(L, Const)	(L, Per)	(L, Event)	(L, Adapt)
Michaelis–Menten ($f(C) = \frac{C}{K+C}$)	(MM, Const)	(MM, Per)	(MM, Event)	(MM, Adapt)
Sigmoidal (Hill) ($f(C) = \frac{C^n}{K^n+C^n}$)	(H, Const)	(H, Per)	(H, Event)	(H, Adapt)
Switch-like ($f(C) = \frac{1}{1+\exp[-\kappa(C-C^*)]}$)	(S, Const)	(S, Per)	(S, Event)	(S, Adapt)

4.5. Regime classification

The post-peak decay rate λ_{decay}, together with the goodness of fit of the exponential approximation, is used to classify the long-term dynamical regime as stable, non-convergent, or oscillatory. This classification is directly linked to the analytical conditions derived in Section 3.2 and provides a consistent bridge between theory and numerical outcomes.

5. Numerical results

In this section, we present the numerical results obtained from the systematic simulation of the sixteen scenarios defined by the combination of four immune response architectures and four exposure profiles. All metrics are computed as described in Section 4, using identical baseline parameters and immune delay $\tau = 2.0$.

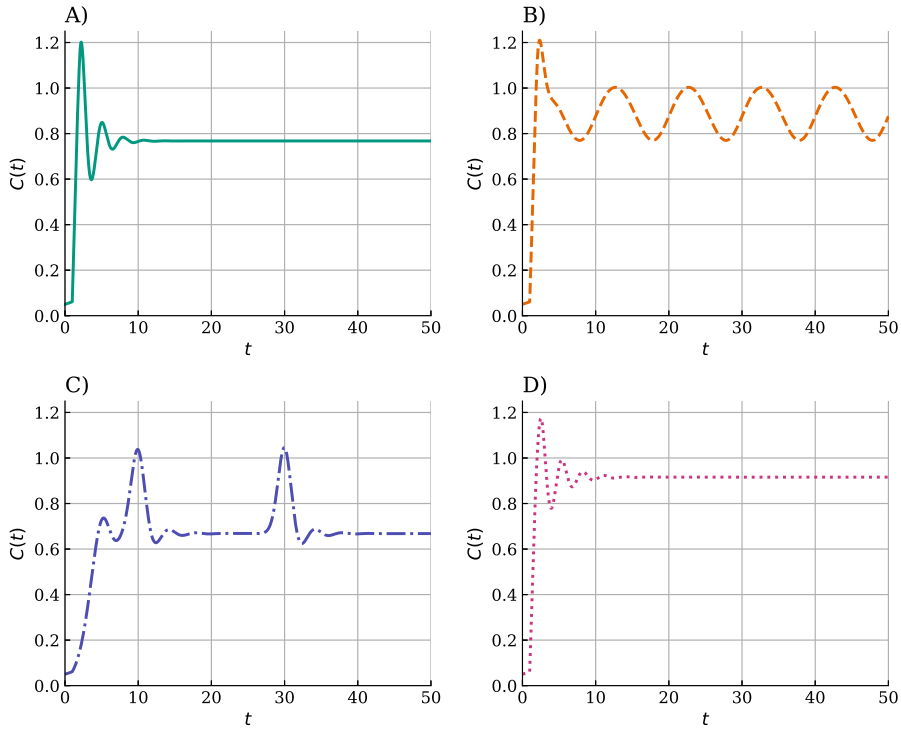

Figure 2. Representative viral load trajectories under different immune response and exposure configurations in the 4×4 factorial framework. (A) Linear immune response with constant exposure, with monotonic convergence toward a steady state. (B) Michaelis–Menten response with periodic exposure, with sustained oscillations driven by delayed immune feedback and external forcing. (C) Hill-type response with event-driven exposure, with pronounced transient peaks following discrete exposure events. (D) Switch-like response with adaptive exposure, with stabilized dynamics under feedback-regulated contact reduction. Simulations are performed using the baseline parameter set reported in Table 3, with identical initial conditions across all panels.

The results are organized to highlight how immune nonlinearity and exposure structure jointly shape (i) early transient amplification, (ii) oscillatory behavior induced by delayed feedback, and (iii) long-term viral persistence and clearance efficiency.

Figure 2 illustrates representative viral load trajectories across immune architectures and exposure profiles. The results indicate distinct dynamical regimes, including monotonic convergence, oscillatory behavior, and transient responses.

Specifically, constant exposure leads to smooth convergence toward equilibrium, whereas periodic forcing induces sustained oscillations consistent with delay-induced Hopf bifurcation. Event-driven exposure generates isolated transient peaks, while adaptive exposure stabilizes the dynamics through feedback mechanisms. These trajectories are consistent with infection patterns reported in within-host viral dynamics studies.

5.1. Peak viral load and early transients

Figure 3 displays the peak viral load $C_{\max}$ across all sixteen scenarios. Across all immune architectures, a robust hierarchy of exposure effects is observed:

$$\text{Constant} > \text{Periodic} > \text{Adaptive} > \text{Event-driven}.$$

Ultrasensitive immune responses (Hill and switch-like) consistently generate higher peaks than linear or Michaelis–Menten responses. This effect is most pronounced under constant and periodic exposure, where delayed immune activation enables substantial early viral amplification. In contrast, event-driven exposure leads to markedly reduced peaks, even for highly nonlinear immune responses, reflecting the transient nature of the forcing.

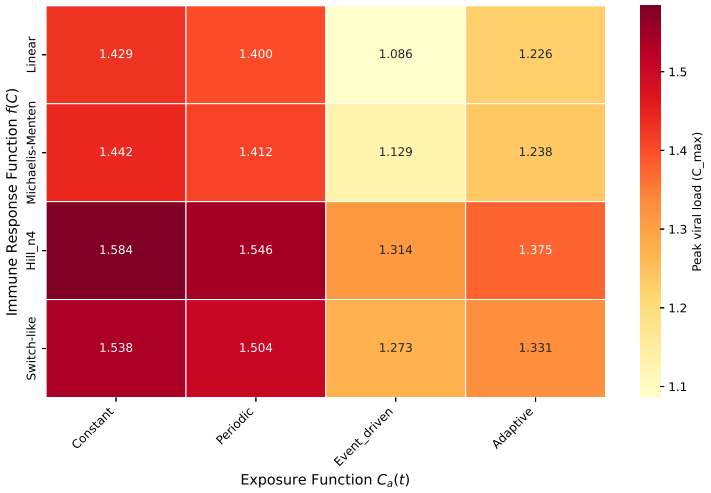

Figure 3. Peak viral load $C_{\max}$ across immune response architectures and exposure profiles. Each bar corresponds to a scenario in the 4×4 factorial design (f, C_a). Exposure structure influences peak values, with constant exposure associated with higher viral loads and event-driven exposure with lower values, while nonlinear immune responses (Hill-type and switch-like) produce higher peaks than linear and Michaelis–Menten responses.

5.2. *Timing metrics: Time to peak and response lag*

The temporal characteristics of infection are summarized by the time to peak $t_{\max}$ and the response lag $\mathcal{L}$ (Figures 4 and 5). Under constant, periodic, and adaptive exposure, the time to peak remains consistently around $t \approx 4$ across all immune architectures.

In contrast, event-driven exposure induces substantially delayed peaks, with $t_{\max}$ exceeding 30 for Michaelis–Menten and switch-like responses. This reflects the dominance of exposure timing over intrinsic viral growth in these scenarios.

The response lag $\mathcal{L}$ further highlights this effect: Event-driven exposure produces the largest lags across all immune functions, consistent with the delayed immune response tracking intermittent external shocks.

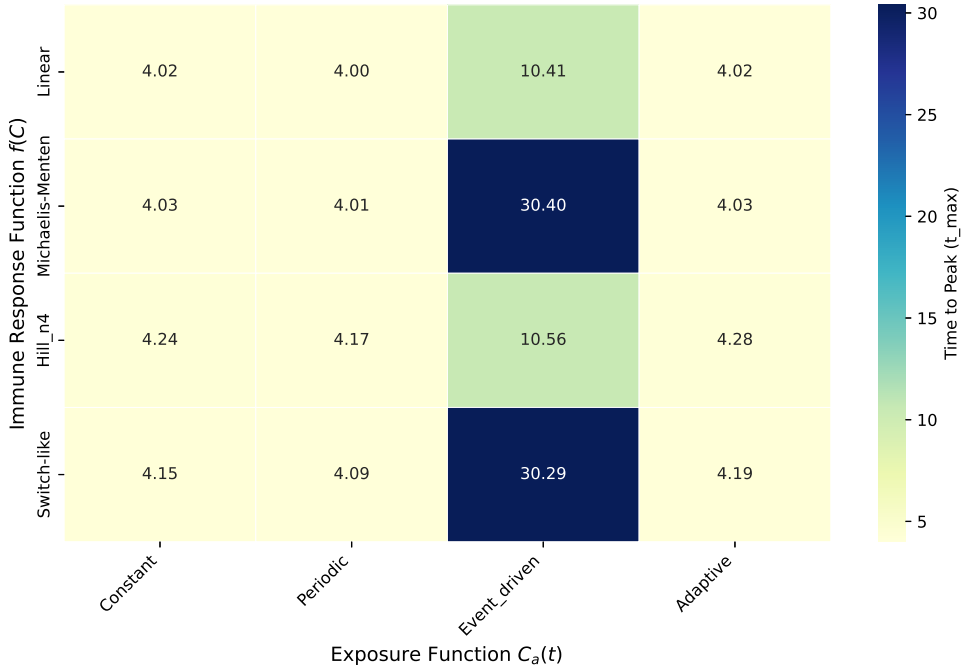

Figure 4. Time to peak viral load $t_{\max}$. Each bar corresponds to a scenario in the 4×4 factorial design (f, C_a). Time to peak remains relatively consistent across most exposure types, whereas event-driven exposure leads to delayed peaks, reflecting the dominant role of exposure timing over intrinsic viral growth.

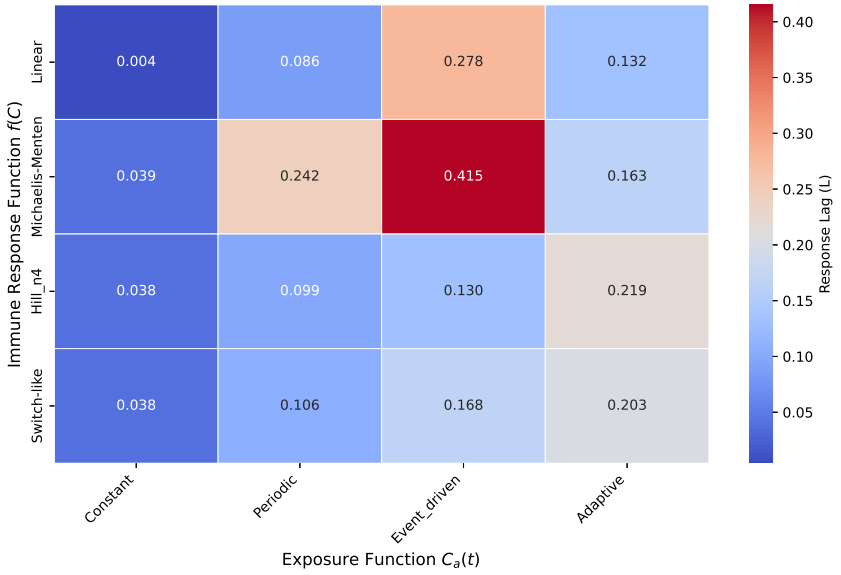

Figure 5. Response lag $\mathcal{L}$ between exposure and viral load. Each bar corresponds to a scenario in the 4×4 factorial design (f, C_a). Event-driven exposure produces the largest lags across all immune responses, consistent with delayed system response to intermittent external forcing, whereas constant and periodic exposure yield shorter and more stable delays.

5.3. Cumulative viral burden

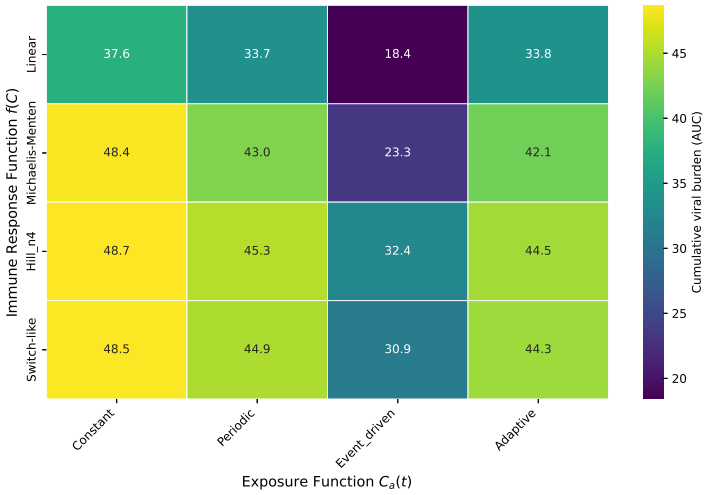

Figure 6. Cumulative viral burden (AUC) across scenarios. Each bar corresponds to a scenario in the 4×4 factorial design (f, C_a). Sustained exposure (constant and periodic) produces higher cumulative burden, whereas event-driven exposure yields lower AUC across all immune responses. Adaptive exposure results in intermediate values, consistent with feedback-regulated contact reducing long-term viral burden despite moderate peak levels.

The cumulative viral burden, measured by the area under the curve (AUC), is shown in Figure 6. Sustained exposure (constant or periodic) yields the largest cumulative burden, particularly for nonlinear immune responses.

Event-driven exposure consistently minimizes AUC across all immune architectures, reducing cumulative burden by up to 50% relative to constant exposure. Adaptive exposure produces intermediate behavior, indicating that feedback-driven reduction of exposure is effective in limiting long-term viral burden, even when peak control is not optimal.

5.4. Oscillatory behavior and dynamical complexity

Figures 7 and 8 quantify oscillatory behavior using the asymptotic amplitude and the number of local maxima. Periodic exposure induces persistent oscillations for all immune responses, with the largest amplitudes observed for Hill and switch-like responses.

Constant and adaptive exposure primarily lead to damped dynamics, while event-driven exposure produces transient oscillations whose number of peaks depends strongly on immune nonlinearity. Highly cooperative responses generate multiple rebounds even in the absence of sustained forcing, highlighting the role of delayed, threshold-like feedback.

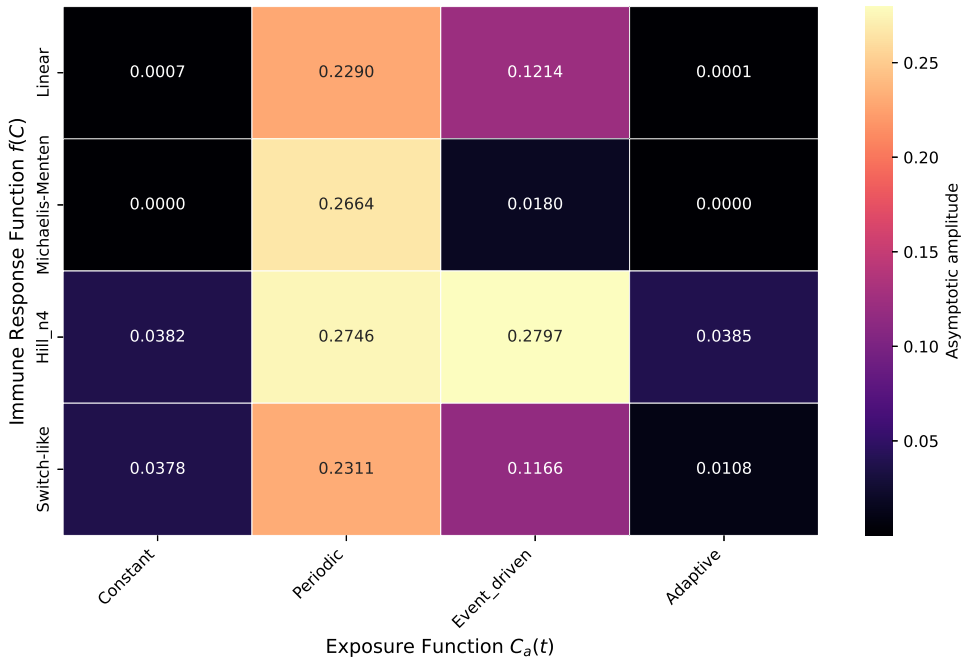

Figure 7. Asymptotic oscillation amplitude. Each bar corresponds to a scenario in the 4×4 factorial design (f, C_a). Periodic exposure produces sustained oscillations across all immune responses, with the largest amplitudes for nonlinear architectures (Hill-type and switch-like), whereas constant and adaptive exposure lead to damped dynamics with near-zero asymptotic amplitude.

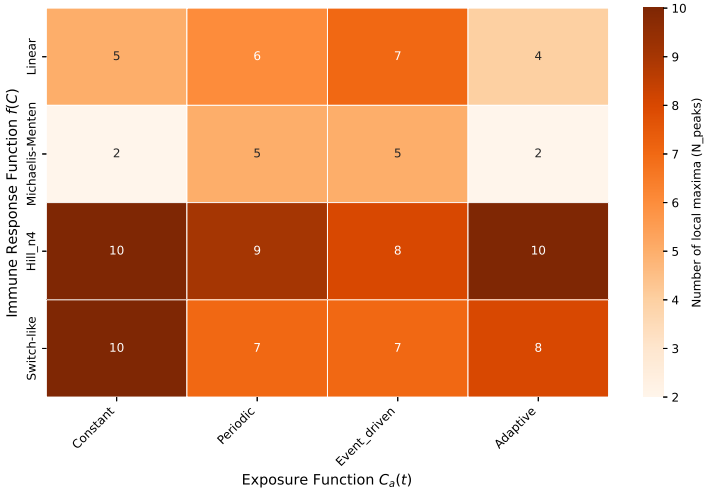

Figure 8. Number of local maxima N_{peaks}. Each bar corresponds to a scenario in the 4×4 factorial design (f, C_a). Periodic exposure and highly nonlinear immune responses are associated with multiple peaks, reflecting sustained or rebound dynamics, whereas constant and adaptive exposure lead to single-peak or weakly oscillatory trajectories.

5.5. *Long-term persistence and clearance efficiency*

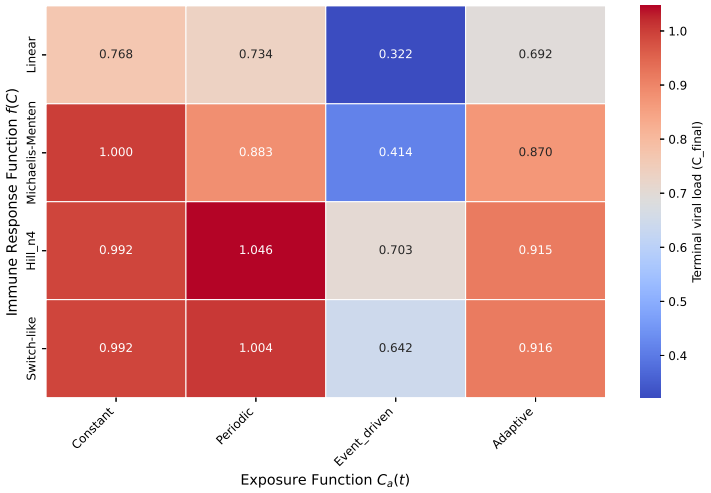

Figure 9. Terminal viral load C_{final}. Each bar corresponds to a scenario in the 4×4 factorial design (f, C_a). Constant exposure is associated with higher terminal viral loads, consistent with persistent infection dynamics, whereas event-driven and adaptive exposure reduce long-term viral levels. Nonlinear immune responses further modulate persistence, with stronger feedback generally associated with lower terminal values.

Terminal viral load and post-peak decay rate provide complementary indicators of long-term control (Figures 9 and 10). Linear and Michaelis–Menten responses under constant exposure

converge exponentially to stable equilibria, as indicated by large positive values of λ_{decay} and high goodness-of-fit. In contrast, periodic and event-driven exposure often produce non-convergent dynamics, reflected by poor exponential fits and near-zero decay rates. Adaptive exposure restores stability for nonlinear immune responses, yielding positive decay rates and reduced terminal viral load.

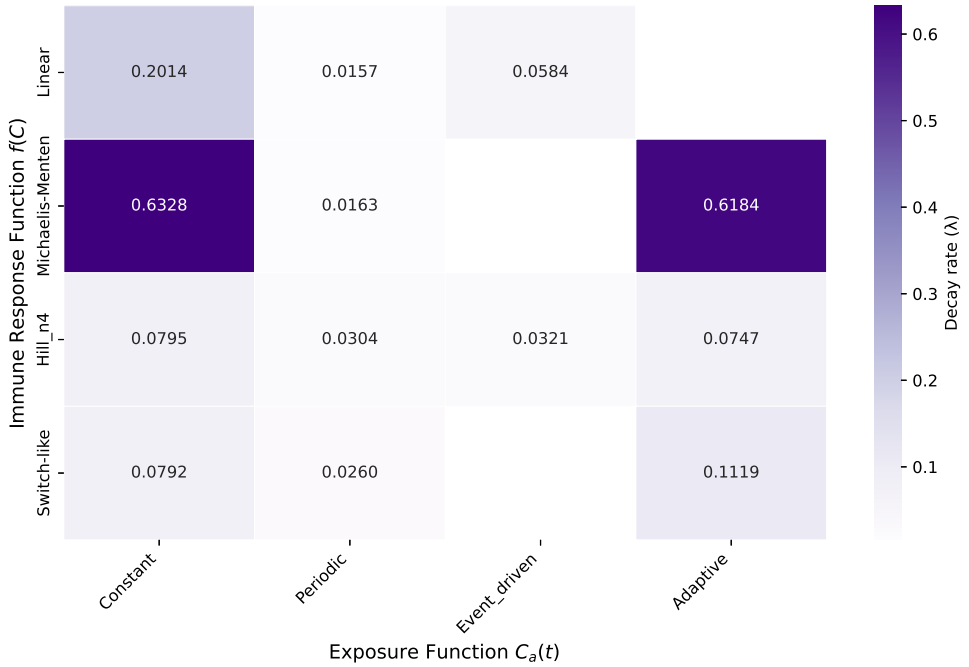

Figure 10. Post-peak decay rate λ_{decay}. Each bar corresponds to a scenario in the 4×4 factorial design (f, C_a). Positive decay rates correspond to stable convergence toward equilibrium, whereas near-zero values are consistent with persistent oscillations or non-convergent dynamics. Linear and Michaelis–Menten responses under constant and adaptive exposure exhibit higher decay rates, while periodic and event-driven exposure reduce convergence and promote sustained dynamics.

5.6. Global regime classification

Figure 11 summarizes the dynamical regimes inferred from the post-peak decay rate and goodness-of-fit criteria. Constant exposure yields stable dynamics across all immune responses. Periodic exposure predominantly leads to non-convergent, oscillatory regimes, while adaptive exposure restores stability for all nonlinear immune functions.

This classification is fully consistent with the analytical Hopf bifurcation conditions derived in Section 3.2.

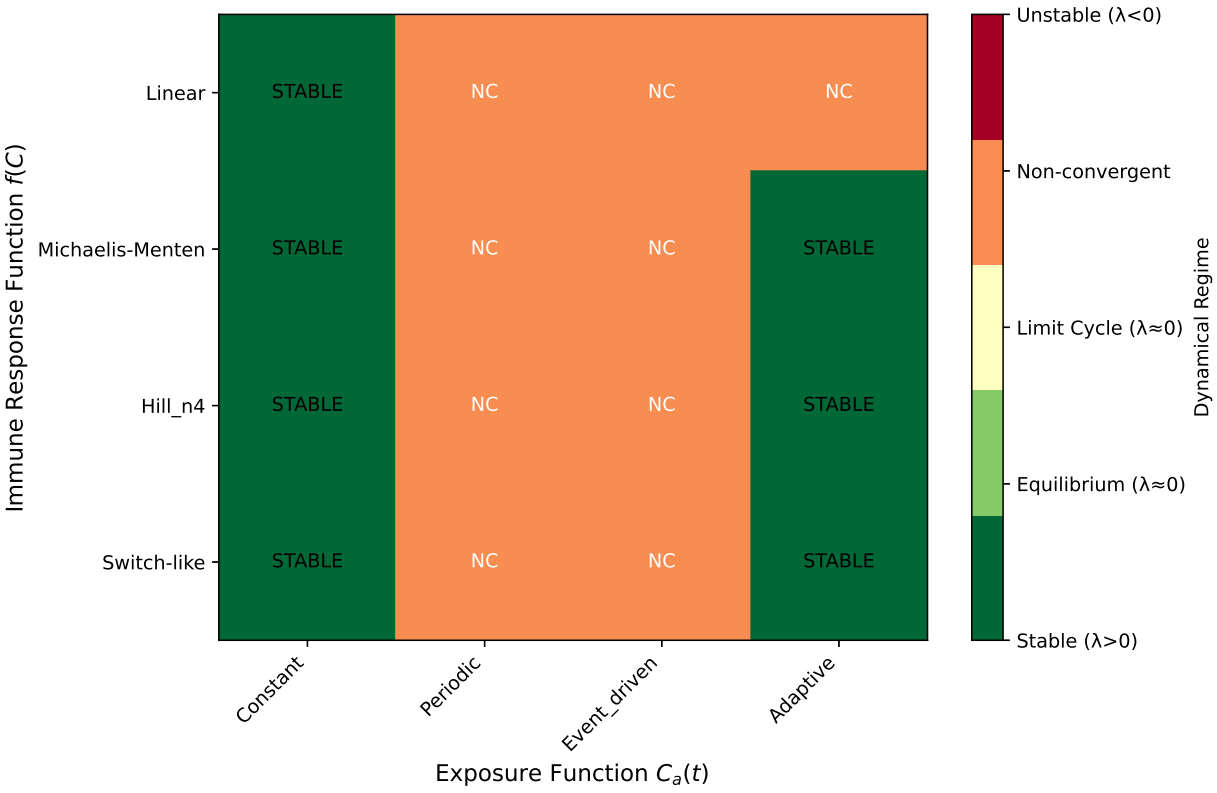

Figure 11. Dynamical regime classification based on λ_{decay} and goodness-of-fit. Each bar corresponds to a scenario in the 4×4 factorial design (f, C_a). Constant exposure is associated with stable dynamics across all immune responses, whereas periodic exposure is associated with non-convergent, oscillatory regimes. Adaptive exposure restores stability for nonlinear immune responses, while event-driven exposure produces intermediate behaviors depending on immune architecture.

5.7. Numerical validation of Hopf bifurcation thresholds

To numerically validate the Hopf bifurcation conditions derived in Section 3, we systematically vary the immune activation delay τ and measure the asymptotic oscillation amplitude of the delayed system. For each immune response architecture, simulations are initialized close to the equilibrium concentration and integrated until transients are eliminated.

Figure 12 shows the resulting bifurcation diagrams. In all cases, oscillations emerge when τ exceeds a critical value, indicating a supercritical Hopf bifurcation. The numerically detected thresholds closely match the theoretical predictions.

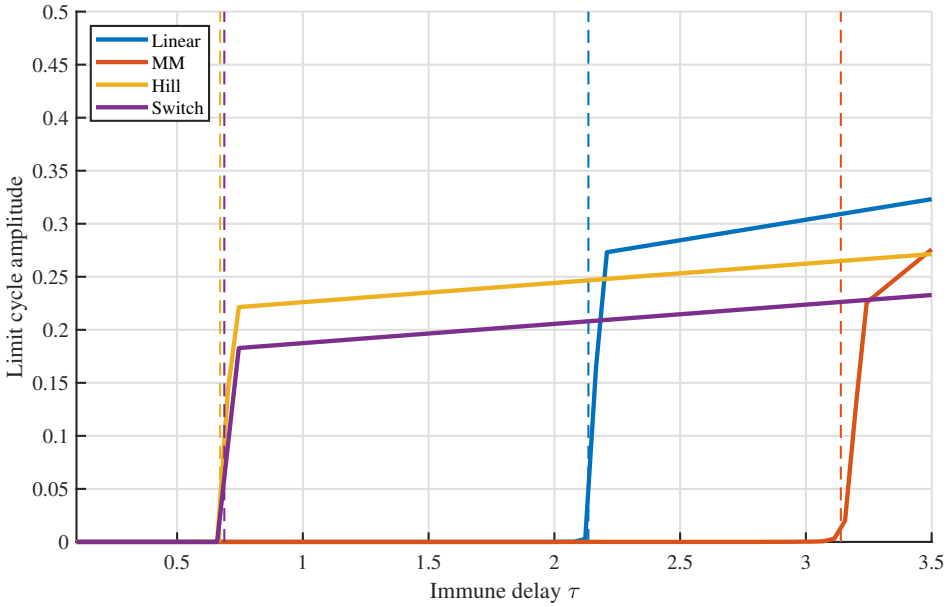

Figure 12. Numerical validation of Hopf bifurcation thresholds across four immune architectures. Solid lines represent the asymptotic oscillation amplitude as a function of the immune delay τ, while vertical dashed lines indicate the theoretical critical thresholds τ_c obtained from linear stability analysis. Ultrasensitive immune responses (Hill-type and switch-like) become unstable at smaller delays ($\tau_c \approx 0.7$) than linear and Michaelis–Menten responses ($\tau_c > 2$), consistent with analytical predictions that increased immune sensitivity lowers the threshold for oscillatory dynamics. Simulations use $r = 1.5$, $\gamma = 3.5$, and $\rho = 0.005$.

5.8. Parameter sensitivity and robustness of immune hierarchy

To assess the robustness of the numerical conclusions, we conduct a parameter sensitivity analysis by independently varying key model parameters (the immune delay τ, immune clearance rate γ, and exposure intensity ρ) by ± 30% around their baseline values. For each parameter combination and immune architecture, we recompute the post-peak decay rate λ_{decay}, peak viral load, cumulative burden, and the presence of sustained oscillations.

Figure 13 summarizes the distribution of λ_{decay} across all parameter combinations. Despite quantitative variability in decay rates, the qualitative hierarchy among immune architectures is preserved across the parameter range: Michaelis–Menten responses consistently exhibit the fastest decay, followed by Hill-type and switch-like responses, while linear immunity remains the least efficient in post-peak control. Implementation details are provided in the Appendix section "Details of the sensitivity analysis".

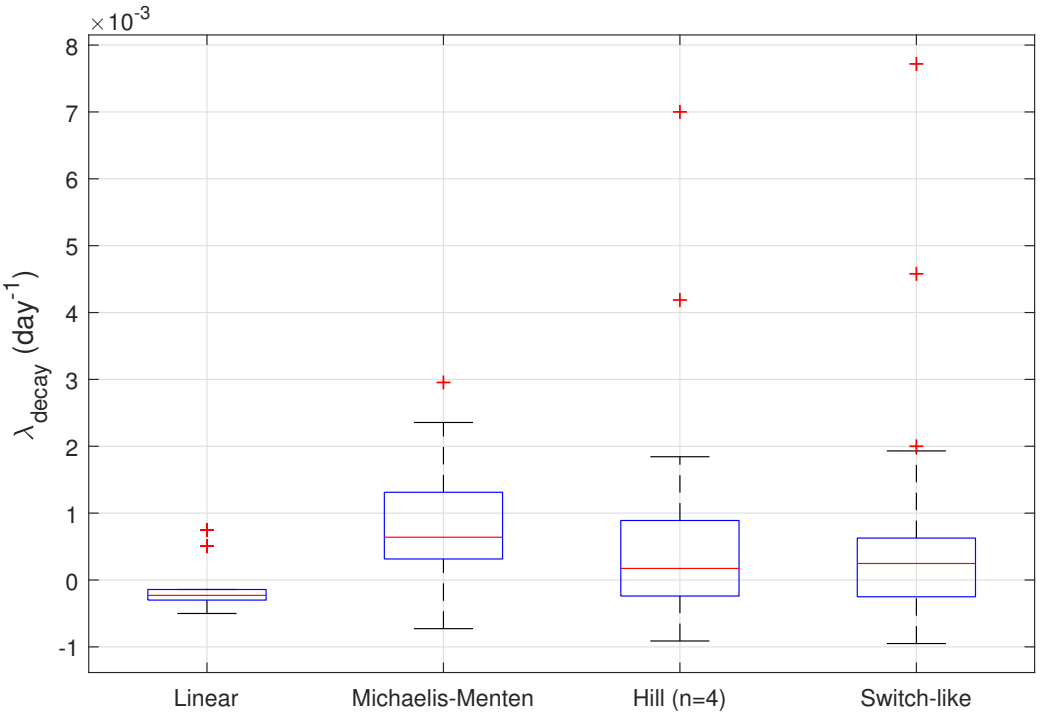

Figure 13. Distribution of the post-peak decay rate λ_{decay} under ± 30% variations of the immune delay τ, clearance rate γ, and exposure magnitude ρ. Each box represents aggregated results across all parameter combinations for a given immune architecture. Although parameter variations introduce quantitative variability, the relative hierarchy of immune responses remains consistent, with Michaelis–Menten responses exhibiting higher decay rates (faster convergence), followed by Hill-type and switch-like responses, while linear immunity is associated with slower decay.

5.9. Clinical consistency of post-peak decay dynamics

To evaluate the biological plausibility of the post-peak decay metric λ_{decay}, we compare model-based decay dynamics with longitudinal viral load data from published clinical cohorts for two pathogens with distinct kinetic profiles: SARS-CoV-2 [43] and Ebola virus (EBOV) [44].

The clinical data used for regression analysis, representing the immune-dominated clearance phase, are detailed in Table 5. For SARS-CoV-2, we utilize Patient 2 data from [43] (days 10–13 post-symptom onset), and for Ebola, we utilize survivor cohort data from [44] (days 9–15). Details of the regression procedure, normalization convention, and data selection used to estimate empirical decay rates are provided in the Appendix section "Details of empirical decay rate estimation".

Table 5. Clinical viral load data points used for empirical decay rate estimation. Viral loads (C) are normalized to the peak value within the observed window [43, 44].

SARS-CoV-2 (Patient 2)		Ebola virus (Survivor)	
Day (t)	Viral load (C)	Day (t)	Viral load (C)
10	1.585	9	0.16500
11	0.100	11	0.04000
12	0.016	13	0.00340
13	0.001	15	0.00017

Linear regression of $\log C(t)$ yields excellent goodness-of-fit for both pathogens ($R^2 > 0.97$), confirming that the post-peak phase is dominated by exponential clearance. The resulting empirical decay rates λ_{emp} and half-lives are summarized in Table 6.

Table 6. Estimated empirical post-peak viral clearance rates and regression statistics.

Pathogen	Regression equation	λ_{emp} (day^{-1})	Half-life (h)	R^2
SARS-CoV-2	$\log C = 24.31 - 2.39t$	2.39	6.9	0.994
Ebola virus	$\log C = 9.01 - 1.16t$	1.16	14.4	0.977

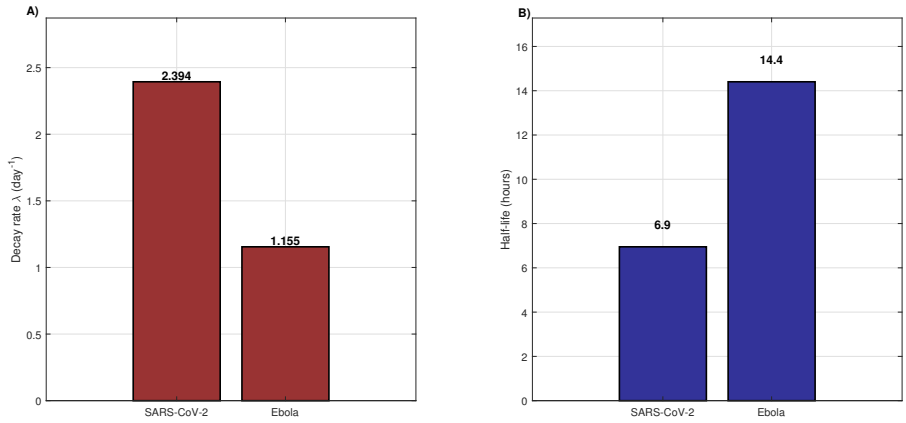

Figure 14. Comparison of empirically derived viral clearance metrics. (A) Estimated post-peak exponential decay rates (λ) in day^{-1}. (B) Corresponding viral clearance half-lives ($t_{1/2}$) in hours. SARS-CoV-2 exhibits a faster clearance rate than Ebola virus, with an approximate twofold increase in λ and a correspondingly shorter half-life, consistent with pathogen-specific differences in post-peak immune control.

As shown in Figure 14, SARS-CoV-2 clears significantly faster than Ebola virus, with calculated half-lives of 6.9 h and 14.4 h, respectively. This empirical ordering mirrors the qualitative hierarchy observed in our DDE simulations: Immune architectures characterized by saturating Michaelis–Menten kinetics (high-efficiency regimes) produce faster decay slopes than ultrasensitive, switch-like architectures (delayed-clearance regimes).

While absolute magnitudes differ due to model normalization, the preservation of this relative ordering across viral species validates λ_{decay} as a biologically grounded proxy for evaluating host-pathogen interaction efficiency.

6. Discussion

In this study, we develop a unified analytical–numerical framework to investigate within-host viral dynamics under delayed immune feedback and heterogeneous exposure, revealing a set of dynamical regimes that extend classical results on delay-induced instability.

Our findings are consistent with the established theory on delayed viral–immune systems, where immune activation delays can destabilize equilibrium states and generate oscillatory dynamics through Hopf bifurcation, as described in [38] and related foundational works [35, 36]. However, our results indicate that these canonical mechanisms persist, and are substantially reshaped, when more realistic, time-dependent exposure patterns are introduced.

A key finding is that external forcing substantially alters the dynamical structure of the system. While constant exposure leads to convergence toward non-zero equilibria and delayed feedback induces oscillations in line with classical theory [1, 2], periodic exposure generates sustained or weakly damped oscillatory dynamics even in parameter regimes that would otherwise be asymptotically stable. This behavior is consistent with forcing-induced transitions and entrainment phenomena observed in epidemiological systems [31, 32]. Importantly, these results indicate that external temporal structure can dominate intrinsic stability properties, effectively overriding equilibrium predictions derived from autonomous models.

The role of immune nonlinearity further amplifies this complexity. Nonlinear response functions, particularly Hill-type and switch-like architectures, introduce ultrasensitivity and threshold effects that significantly enhance transient amplification and promote oscillatory behavior under delayed feedback. This mechanism is consistent with nonlinear immune modeling frameworks [**?**] and theoretical descriptions of ultrasensitivity and bistability [29]. Crucially, our results suggest that immune nonlinearity acts synergistically with exposure structure: Its destabilizing effects are strongly modulated by the temporal organization of exposure. In particular, even highly nonlinear immune responses remain effectively controlled under intermittent or adaptive exposure, indicating that external forcing can mitigate intrinsic nonlinear amplification.

Taken together, these results suggest that exposure timing, rather than cumulative exposure alone, plays a dominant role in shaping within-host viral burden and persistence. Event-driven exposure consistently reduces cumulative viral burden and peak amplification, despite inducing delayed responses and complex transient dynamics. Similarly, adaptive exposure, representing behavioral feedback such as risk avoidance or self-regulation, emerges as a stabilizing mechanism that suppresses oscillations and limits viral persistence. These results align with behavioral epidemiology models [19, 34] and provide a mechanistic interpretation at the within-host level.

Taken together, these mechanisms highlight the coupled role of immune dynamics and exposure timing in shaping infection outcomes.

A central methodological contribution of this work is the introduction of the post-peak decay rate λ_{decay} as a unified quantitative proxy for asymptotic dynamics. Unlike classical stability analysis based on linearization and eigenvalues, which is limited to autonomous systems near equilibrium, the

proposed metric applies to non-autonomous, nonlinear, and oscillatory regimes. By estimating the exponential rate of convergence of the deviation $|C(t) - C^*|$, where C^* denotes the asymptotic state, this approach provides a consistent measure of stability across dynamical behaviors. In particular, it enables discrimination between convergence to equilibrium, damped oscillations, and persistent non-decaying regimes, thereby bridging analytical stability theory with data-driven numerical diagnostics. Similar decay-based measures have been used in within-host modeling and experimental studies [5, 45], supporting the biological relevance of this framework.

Taken together, these results reveal a systematic trade-off between transient amplification and long-term control in delayed immune systems. Highly sensitive immune responses can enhance late-stage regulation but may enable substantial early viral expansion when activation is delayed. Conversely, temporally structured exposure, particularly intermittent or adaptive patterns, can compensate for intrinsic immune limitations, reducing overall viral burden even in the presence of delayed feedback. From a modeling perspective, these findings emphasize that immune architecture, delay, and exposure cannot be analyzed independently without risking qualitatively misleading conclusions. In particular, neglecting exposure structure may obscure key mechanisms underlying oscillatory behavior, persistence, and stabilization.

A limitation of this framework is its deterministic nature, which does not capture stochastic extinction at low viral loads or variability due to heterogeneous immune responses. The immune delay is modeled as a discrete lag, which may oversimplify its distributed biological nature. In addition, exposure functions are imposed exogenously, without mechanistic coupling to behavioral or transmission processes. Extending the model to incorporate stochasticity, distributed delays, and multiscale host–environment interactions represents an important direction for future research.

From a biological and clinical perspective, the dynamical regimes identified in this study are consistent with reported within-host viral kinetics across infections. Longitudinal analyses of SARS-CoV-2 and influenza indicate that viral load rises rapidly to a peak prior to the onset of effective adaptive immunity, followed by a slower, approximately exponential decay phase [46–48]. This temporal structure supports the assumption of delayed immune activation and provides a mechanistic interpretation of the post-peak decay rate λ_{decay} as a proxy for immune-mediated clearance efficiency, consistent with that in Section 5.9.

Clinical and modeling studies also show that the timing and strength of immune responses determine infection outcomes. Delayed or weaker immune activation is associated with higher peak viral loads, prolonged infection, and increased variability, whereas earlier or stronger responses lead to reduced peaks and faster clearance [49–51]. These observations align with our results, where ultrasensitive immune architectures amplify transient viral peaks without necessarily improving long-term clearance. In addition, heterogeneous exposure and repeated viral intake modulate within-host dynamics, including synchronization effects, peak amplification, and viral persistence, depending on exposure timing [52]. This is consistent with our finding that exposure structure, rather than total exposure magnitude, plays a key role in shaping infection dynamics.

Overall, variability in patient-level viral trajectories, including viral rebound, prolonged shedding, and oscillatory behavior, can be explained by the combined effects of delayed immune feedback and time-dependent exposure. Such mechanisms have been reported in SARS-CoV-2 and other viral infections, where multiple peaks, delayed clearance, and heterogeneous outcomes arise from differences in immune timing and host–pathogen interactions [53, 54].

In summary, we extend the classical delayed viral–immune theory by incorporating heterogeneous exposure, identify robust dynamical regimes across immune architectures, and introduce a generalizable decay-based framework for regime classification. These results provide a unified framework for understanding how immune delay and exposure structure jointly shape within-host viral dynamics.

7. Conclusions

In this study, we developed a delayed within-host viral dynamics model incorporating nonlinear immune responses and heterogeneous exposure. The analysis revealed how immune sensitivity and exposure structure jointly shape viral persistence, transient amplification, and oscillatory behavior. In particular, the proposed 4×4 factorial framework enabled a systematic comparison of sixteen dynamical scenarios, supported by theoretical results on stability and delay-induced Hopf bifurcations.

From a biological perspective, the results indicate that delayed immune activation may destabilize viral control, while intermittent or adaptive exposure can reduce long-term persistence. These findings highlight the importance of timing and feedback mechanisms in infection dynamics.

Researchers may extend this framework to stochastic formulations, multi-scale coupling with population dynamics, or patient-specific parameter estimation.

Use of AI tools declaration

The authors declare they have not used Artificial Intelligence (AI) tools in the creation of this article.

Conflict of interest

The authors declare there is no conflict of interest.

Code availability

Numerical simulations and analyses were conducted using a combination of MATLAB and Python scripts. The complete, reproducible implementation is available in Python at: https://github.com/abdelkarimlamghari/viral-dynamics-dde.

References

1. M. A. Nowak, R. M. May, *Virus Dynamics: Mathematical Principles of Immunology and Virology*, Oxford University Press, Oxford, 2000. https://doi.org/10.1093/oso/9780198504184.001.0001
2. A. S. Perelson, Modelling viral and immune system dynamics, *Nat. Rev. Immunol.*, **2** (2002), 28–36. https://doi.org/10.1038/nri700
3. A. S. Perelson, A. U. Neumann, M. Markowitz, J. M. Leonard, D. D. Ho, HIV-1 dynamics in vivo: Virion clearance rate, infected cell life-span and viral generation time, *Science*, **271** (1996), 1582–1586. https://doi.org/10.1126/science.271.5255.1582

4. A. S. Perelson, R. M. Ribeiro, Modeling the within-host dynamics of HIV infection, *BMC Biol.*, **11** (2013), 96. https://doi.org/10.1186/1741-7007-11-96
5. K. A. Pawelek, G. T. Huynh, M. Quinlivan, A. Cullinane, L. Rong, A. S. Perelson, Modeling within-host dynamics of influenza virus infection including immune responses, *PLoS Comput. Biol.*, **8** (2012), e1002588. https://doi.org/10.1371/journal.pcbi.1002588
6. H. Song, W. Jiang, S. Liu, Virus dynamics model with intracellular delays and immune response, *Math. Biosci. Eng.*, **12**(1) (2015), 185–208. https://doi.org/10.3934/mbe.2015.12.185
7. G. Dagasso, J. Urban, M. Kwiatkowska, Incorporating time delays in the mathematical modelling of the human immune response in viral infections, *Procedia Comput. Sci.*, **185** (2021), 144–151. https://doi.org/10.1016/j.procs.2021.05.016
8. B. Wacker, Revisiting the classical target cell limited dynamical within-host HIV model: Basic mathematical properties and stability analysis, *Math. Biosci. Eng.*, **21** (2024), 7805–7829. https://doi.org/10.3934/mbe.2024343
9. I. Ghosh, Within host dynamics of SARS-CoV-2 in humans: Modeling immune responses and antiviral treatments, *SN Comput. Sci.*, **2** (2021), 482. https://doi.org/10.1007/s42979-021-00919-8
10. Z. Zhou, D. Li, Z. Zhao, S. Shi, J. Wu, J. Li, et al., Dynamical modelling of viral infection and cooperative immune protection in COVID-19 patients, *PLoS Comput. Biol.*, **19** (2023), e1011383. https://doi.org/10.1371/journal.pcbi.1011383
11. N. K. Vaidya, A. Bloomquist, A. S. Perelson, Modeling within-host dynamics of SARS-CoV-2 infection: A case study in ferrets, *Viruses*, **13** (2021), 1635. https://doi.org/10.3390/v13081635
12. J. E. Forde, *Delay Differential Equation models in Mathematical Biology*, Ph.D. thesis, University of Michigan, 2005.
13. L. Rong, A. S. Perelson, Modeling latently infected cell activation: Viral and latent reservoir persistence, and viral blips in HIV-infected patients on potent therapy, *PLoS Comput. Biol.*, **5** (2009), e1000533. https://doi.org/10.1371/journal.pcbi.1000533
14. P. W. Nelson, A. S. Perelson, Mathematical analysis of delay differential equation models of HIV-1 infection, *Math. Biosci.*, **179** (2002), 73–94. https://doi.org/10.1016/S0025-5564(02)00099-8
15. Z. Hu, J. Yang, Q. Li, S. Liang, D. Fan, Mathematical analysis of stability and Hopf bifurcation in a delayed HIV infection model with saturated immune response, *Math. Methods Appl. Sci.*, **47** (2024), 9834–9857. https://doi.org/10.1002/mma.10097
16. A. Goyal, D. B. Reeves, E. F. Cardozo-Ojeda, J. T. Schiffer, B. T. Mayer, Viral load and contact heterogeneity predict SARS-CoV-2 transmission and super-spreading events, *eLife*, **10** (2021), e63537. https://doi.org/10.7554/eLife.63537
17. N. G. Davies, P. Klepac, Y. Liu, K. Prem, M. Jit, R. M. Eggo, Age-dependent effects in the transmission and control of COVID-19 epidemics, *Nat. Med.*, **26** (2020), 1205–1211. https://doi.org/10.1038/s41591-020-0962-9
18. O. Puhach, K. Adea, N. Hulo, P. Sattonnet, C. Genecand, A. Iten, et al., Infectious viral load in unvaccinated and vaccinated individuals infected with ancestral, Delta or Omicron SARS-CoV-2, *Nat. Med.*, **28** (2022), 1491–1500. https://doi.org/10.1038/s41591-022-01816-0

19. A. Bouchnita, A. Jebrane, A hybrid multi-scale model of COVID-19 transmission dynamics to assess the potential of non-pharmaceutical interventions, *Chaos Solitons Fractals*, **138** (2020), 109941. https://doi.org/10.1016/j.chaos.2020.109941

20. A. Lamghari, D. S. I. Kanté, A. Jebrane, A. Hakim, Modeling the impact of distancing measures on infectious disease spread: A case study of COVID-19 in the Moroccan population, *Math. Biosci. Eng.*, **21** (2024), 4370–4396. https://doi.org/10.3934/mbe.2024193

21. D. S. I. Kanté, A. Jebrane, A. Bouchnita, A. Hakim, Estimating the risk of contracting COVID-19 in different settings using a multiscale transmission dynamics model, *Mathematics*, **11** (2023), 254. https://doi.org/10.3390/math11010254

22. G. McCarthy, H. M. Dobrovolny, Determining the best mathematical model for implementation of non-pharmaceutical interventions, *Math. Biosci. Eng.*, **22** (2025), 700–724. https://doi.org/10.3934/mbe.2025026

23. K. Ngoun, N. Alvarez, A. Awad, H. Ryu, Immune dysregulation in COVID-19: Mathematical modeling of the within-host dynamics, *Math. Biosci. Eng.*, **23** (2026), 987–1049. https://doi.org/10.3934/mbe.2026038

24. P. Baccam, C. Beauchemin, C. A. Macken, F. G. Hayden, A. S. Perelson, Kinetics of influenza a virus infection in humans, *J. Virol.*, **80** (2006), 7590–7599. https://doi.org/10.1128/JVI.01623-05

25. R. Ke, C. Zitzmann, D. D. Ho, R. M. Ribeiro, A. S. Perelson, In vivo kinetics of SARS-CoV-2 infection and its relationship with a person's infectiousness, *Proc. Natl. Acad. Sci. U.S.A.*, **118** (2021), e2111477118. https://doi.org/10.1073/pnas.2111477118

26. K. S. Kim, K. Ejima, S. Iwanami, Y. Fujita, H. Ohashi, Y. Koizumi, et al., A quantitative model used to compare within-host SARS-CoV-2, MERS-CoV and SARS-CoV dynamics provides insights into the pathogenesis and treatment of SARS-CoV-2, *PLoS Biol.*, **19** (2021), e3001128. https://doi.org/10.1371/journal.pbio.3001128

27. G. A. Bocharov, A. A. Romanyukha, Mathematical model of antiviral immune response. III. Influenza A virus infection, *J. Theor. Biol.*, **167**(4) (1994), 323–360. https://doi.org/10.1006/jtbi.1994.1074

28. D. Wodarz, *Killer Cell Dynamics: Mathematical and Computational Approaches to Immunology*, Springer-Verlag, New York, 2007. https://doi.org/10.1007/978-0-387-68733-9

29. J. E. Ferrell, S. H. Ha, Ultrasensitivity part I: Michaelian responses and zero-order ultrasensitivity, *Trends Biochem. Sci.*, **39** (2014), 496–503. https://doi.org/10.1016/j.tibs.2014.08.003

30. K. Guram, S. S. Kim, V. Wu, P. D. Sanders, S. Patel, S. P. Schoenberger, et al., A threshold model for T-cell activation in the era of checkpoint blockade immunotherapy, *Front. Immunol.*, **10** (2019), 491. https://doi.org/10.3389/fimmu.2019.00491

31. D. J. D. Earn, P. Rohani, B. M. Bolker, B. T. Grenfell, A simple model for complex dynamical transitions in epidemics, *Science*, **287** (2000), 667–670. https://doi.org/10.1126/science.287.5453.667

32. S. Altizer, A. Dobson, P. Hosseini, P. Hudson, M. Pascual, P. Rohani, Seasonality and the dynamics of infectious diseases, *Ecol. Lett.*, **9** (2006), 467–484. https://doi.org/10.1111/j.1461-0248.2005.00879.x

33. S. Setianto, D. Hidayat, Modeling the time-dependent transmission rate using Gaussian pulses for analyzing the COVID-19 outbreaks in the world, *Sci. Rep.*, **13** (2023), 4466. https://doi.org/10.1038/s41598-023-31714-5

34. S. Funk, E. Gilad, C. Watkins, V. A. A. Jansen, The spread of awareness and its impact on epidemic outbreaks, *Proc. Natl. Acad. Sci. U.S.A.*, **106** (2009), 6872–6877. https://doi.org/10.1073/pnas.0810762106

35. Y. Kuang, *Delay Differential Equations with Applications in Population Dynamics*, Academic Press, Boston, MA, 1993.

36. J. K. Hale, S. M. Verduyn Lunel, *Introduction to Functional Differential Equations*, Springer-Verlag, New York, 1993. https://doi.org/10.1007/978-1-4612-4342-7

37. C. L. Dym, *Principles of Mathematical Modeling*, 2nd edition, Elsevier Academic Press, Amsterdam, 2004.

38. T. Erneux, *Applied Delay Differential Equations*, Springer, New York, 2009. https://doi.org/10.1007/978-0-387-74372-1

39. E. Zeidler, *Nonlinear Functional Analysis and its Applications I: Fixed-Point Theorems*, Springer, New York, 1986.

40. A. Handel, I. M. Longini, R. Antia, Towards a quantitative understanding of the within-host dynamics of influenza A infections, *J. R. Soc. Interface*, **7** (2010), 35–47. https://doi.org/10.1098/rsif.2009.0067

41. A. Iggidr, J. Mbang, G. Sallet, Stability analysis of within-host parasite models with delays, *Math. Biosci.*, **209** (2007), 51–75. https://doi.org/10.1016/j.mbs.2007.01.008

42. C. Li, J. Xu, J. Liu, Y. Zhou, The within-host viral kinetics of SARS-CoV-2, *Math. Biosci. Eng.*, **17** (2020), 2853–2861. https://doi.org/10.3934/mbe.2020159

43. F. X. Lescure, L. Bouadma, D. Nguyen, M. Parisey, P. H. Wicky, S. Behillil, et al., Clinical and virological data of the first cases of COVID-19 in Europe: A case series, *Lancet Infect. Dis.*, **20** (2020), 697–706. https://doi.org/10.1016/S1473-3099(20)30200-0

44. A. K. McElroy, R. S. Akondy, D. R. McIlwain, H. Chen, Z. Bjornson-Hooper, N. Mukherjee, et al., Immunologic timeline of Ebola virus disease and recovery in humans, *JCI Insight*, **5** (2020), e137260. https://doi.org/10.1172/jci.insight.137260

45. J. D. Challenger, C. Y. Foo, Y. Wu, A. W. C. Yan, M. Moradi Marjaneh, F. Liew, et al., Modelling upper respiratory viral load dynamics of SARS-CoV-2, *BMC Med.*, **20**(1) (2022), 25. https://doi.org/10.1186/s12916-021-02220-0

46. H. C. Stankiewicz Karita, T. Q. Dong, C. Johnston, K. M. Neuzil, M. K. Paasche-Orlow, P. J. Kissinger, et al., Trajectory of viral RNA load among persons with incident SARS-CoV-2 G614 infection (Wuhan strain) in association with COVID-19 symptom onset and severity, *JAMA Netw. Open*, **5** (2022), e2142796. https://doi.org/10.1001/jamanetworkopen.2021.42796

47. S. A. Iyaniwura, R. M. Ribeiro, C. Zitzmann, T. Phan, R. Ke, A. S. Perelson, The kinetics of SARS-CoV-2 infection based on a human challenge study, *Proc. Natl. Acad. Sci.*, **121** (2024), e2406303121. https://doi.org/10.1073/pnas.2406303121

48. C. Hadjichrysanthou, S. Cauchemez, M. Baguelin, Within-host dynamics of influenza A virus, *J. R. Soc. Interface*, **13** (2016), 20160289. https://doi.org/10.1098/rsif.2016.0289

49. K. Owens, S. Esmaeili, J. T. Schiffer, Heterogeneous SARS-CoV-2 kinetics due to variable timing and intensity of immune responses, *JCI Insight*, **9** (2024), e176286. https://doi.org/10.1172/jci.insight.176286

50. J. A. Hay, S. M. Kissler, J. R. Fauver, C. Mack, C. G. Tai, R. M. Samant, et al., Quantifying the impact of immune history and variant on SARS-CoV-2 viral kinetics and infection rebound: A retrospective cohort study, *eLife*, **11** (2022), e81849. https://doi.org/10.7554/eLife.81849

51. M. Koutsakos, W. S. Lee, A. Reynaldi, H.-X. Tan, G. Gare, P. Kinsella, et al., The magnitude and timing of recalled immunity after breakthrough infection is shaped by SARS-CoV-2 variants, *Immunity*, **55** (2022), 1316–1326.e4. https://doi.org/10.1016/j.immuni.2022.05.018

52. P. Cao, A. W. C. Yan, J. M. Heffernan, S. Petrie, R. G. Moss, L. A. Carolan, et al., Innate immunity and the inter-exposure interval determine the dynamics of secondary influenza virus infection and explain observed viral hierarchies, *PLoS Comput. Biol.*, **11** (2015), e1004334. https://doi.org/10.1371/journal.pcbi.1004334

53. B. Chatterjee, H. S. Sandhu, N. M. Dixit, Modeling recapitulates the heterogeneous outcomes of SARS-CoV-2 infection and quantifies the differences in the innate immune and CD8 T-cell responses between patients experiencing mild and severe symptoms, *PLoS Pathog.*, **18** (2022), e1010630. https://doi.org/10.1371/journal.ppat.1010630

54. R. Ke, P. P. Martinez, R. L. Smith, L. L. Gibson, A. Mirza, M. Conte, et al., Daily longitudinal sampling of SARS-CoV-2 infection reveals substantial heterogeneity in infectiousness, *Nat. Microbiol.*, **7** (2022), 640–652. https://doi.org/10.1038/s41564-022-01105-z

Appendix

All exposure functions reported below correspond to the normalized forms used in numerical simulations, with parameters chosen to be consistent with the baseline values defined in Table 3. In particular, exposure amplitudes are scaled relative to the reference level C_0, such that $C_a(t) = 1$ corresponds to $C_a(t) = C_0$ in the main model. Similarly, immune response parameters (K, n, κ, C^*) take the fixed values reported in Table 3.

Table A1. Mathematical forms of the exposure functions $C_a(t)$ used in the 16 simulated scenarios. All functions are shown in normalized form, with parameter values corresponding to $C_0 = 1$, $\eta = 0.5$, $\omega = 2\pi/10$, pulse centers $t_e = \{10, 30\}$, and pulse variance $\sigma^2 = 1$.

Label	Analytical form of $C_a(t)$	Interpretation
Constant	$C_a(t) = 1$	Persistent background exposure
Periodic	$C_a(t) = \frac{1}{2}\left(1.5 + 0.5\sin\left(\frac{2\pi t}{10}\right)\right)$	Seasonal or rhythmic contact patterns
Event-driven	$C_a(t) = \exp\left(-\frac{(t-10)^2}{2}\right) + \exp\left(-\frac{(t-30)^2}{2}\right)$	Discrete exposure events (e.g., gatherings)
Adaptive	$C_a(t) = \frac{1}{1+0.5\,C(t)}$	Behavioral response reducing exposure based on current viral load

Table A2. Mathematical forms of the immune response functions $f(C)$ used in the model. Parameter values are fixed across all simulations: $K = 0.5$, $n = 4$, $\kappa = 10$, and $C^* = 0.5$.

Label	Analytical form of $f(C)$	Biological interpretation
Linear	$f(C) = C$	Proportional clearance; baseline immune response
Michaelis–Menten	$f(C) = \dfrac{C}{K + C}$	Saturating immune response due to limited effector capacity
Hill-type (sigmoidal)	$f(C) = \dfrac{C^n}{K^n + C^n}$	Cooperative activation; ultrasensitivity (Hill coefficient $n = 4$)
Switch-like	$f(C) = \dfrac{1}{1 + \exp[-\kappa(C - C^*)]}$	Threshold-driven activation; all-or-none immune switch

Details of empirical decay rate estimation

Empirical post-peak decay rates were estimated using linear regression of the log-transformed viral load during the clearance phase, assuming an exponential decay of the form

$$C(t) = C_0 \exp(-\lambda t).$$

Taking the natural logarithm yields

$$\log C(t) = \log C_0 - \lambda t,$$

from which the decay rate λ is obtained as the negative slope of the least-squares linear fit.

Only data points corresponding to the monotonic post-peak decline are used, as specified in Table 5. Viral loads are normalized to the maximum observed value within each patient window to remove scale dependence and ensure comparability across datasets.

Details of the sensitivity analysis

The sensitivity analysis explored all combinations of τ, γ, and ρ varied by ± 30% around baseline values. For each configuration, metrics were computed from numerical trajectories using identical procedures to the baseline simulations. A total of 108 simulations per immune architecture were performed.

AIMS Press